Heat exchange performance evaluation inside a lattice panel using CFD analysis for an innovative aerospace anti-icing system

Aerospace Science and Technology 141 (2023) 108565

Contents lists available at ScienceDirect

Aerospace Science and Technology

journal homepage: www.elsevier.com/locate/aescte

Heat exchange performance evaluation inside a lattice panel using CFD analysis for an innovative aerospace anti-icing system ☆

Carlo Giovanni Ferro *, Francesco Pietrangelo, Paolo Maggiore

Politecnico di Torino, Corso Duca degli Abruzzi, Torino, 10124, Italy

ARTICLE INFO

Article history:
Received 17 May 2023
Received in revised form 4 July 2023
Accepted 4 August 2023
Available online 9 August 2023
Communicated by Damiano Casalino

Keywords:
Additive manufacturing (AM)
Selective laser melting (SLM)
Anti-icing systems
Lattice structures
CFD analysis
Design of experiment

ABSTRACT

As the global push for sustainable development intensifies, the aerospace industry is exploring innovative solutions to reduce greenhouse gas emissions and optimize resource consumption. This paper investigates the performance of an advanced anti-icing system that integrates an onboard function within the primary structure of an aircraft, offering potential reductions in weight, cost, and energy consumption. To evaluate the heat exchange performance of this innovative system, we examine various lattice structures featuring different cell topologies, sizes, and densities. High-fidelity Computational Fluid Dynamics (CFD) simulations are utilized to assess the performance of the constituent cells within the lattice panel, with the goal of identifying the optimal solution that meets design requirements for heat transfer efficiency, pressure, and overall mass of the components. A statistical approach based on Design of Experiments (DoE) is employed to elucidate the relationship between the cell design parameters and the resulting thermal properties. Our findings contribute valuable insights for the development and implementation of advanced aerospace anti-icing systems, supporting the ongoing evolution of sustainable and efficient aviation technologies.

1. Introduction

The urgent need to address climate change and promote sustainable development has led to a growing focus on reducing greenhouse gas emissions and optimizing resource consumption across various industries, including aerospace [1], [2]. Aircraft performance and efficiency have become critical factors as the aviation industry faces increasing pressure to minimize its environmental impact [3], [4]. In recent years, researchers have sought to develop innovative anti-icing systems that improve aircraft performance while reducing weight, cost, and energy consumption [5], [6]. According to the state of the art there are several types of anti-icing systems used in aircraft, including thermal anti-icing systems that utilize hot air bleed from the engines, electromechanical expulsion de-icing systems, pneumatic boot systems that use air pressure to break up ice, and chemical anti-icing systems that disperse de-icing fluids to prevent ice build-up on the aircraft's surfaces.

One such promising approach is the integration of anti-icing systems within the primary structure of an aircraft [7], [8]. Such integration could offer a myriad of advantages including cost and energy efficiency, reduced power requirements, and overall enhanced system performance; nevertheless, potential challenges such as increased design complexity and manufacturing precision needs could pose disadvantages that require careful consideration during development.

Lattice structures, which have been widely studied for their lightweight and high strength-to-weight ratio [9], [10], can be employed in the design of such integrated anti-icing systems. Various lattice structures featuring different cell topologies, sizes, and densities have been proposed to optimize heat exchange performance [11], [12].

Computational Fluid Dynamics (CFD) analysis has proven to be an invaluable tool for the assessment and optimization of heat transfer performance in aerospace applications [13]. High-fidelity CFD simulations can effectively evaluate the performance of different lattice structures and cell configurations within the context of an integrated anti-icing system [14].

To further understand the relationship between cell design parameters and the resulting thermal properties, a statistical approach based on Design of Experiments (DoE) has been employed [15], [16]. DoE offers a systematic methodology for identifying op-

☆ Please cite this article as: Ferro et al., Heat Exchange Performance Evaluation Inside a Lattice Panel Using CFD Analysis for an Innovative Aerospace Anti-Icing System. Aerospace Science and Technology (2023), http://dx.doi.org/10.1016/j.cviu.2017.00.000.

* Corresponding author.
E-mail address: carlo.ferro@polito.it (C.G. Ferro).

https://doi.org/10.1016/j.ast.2023.108565

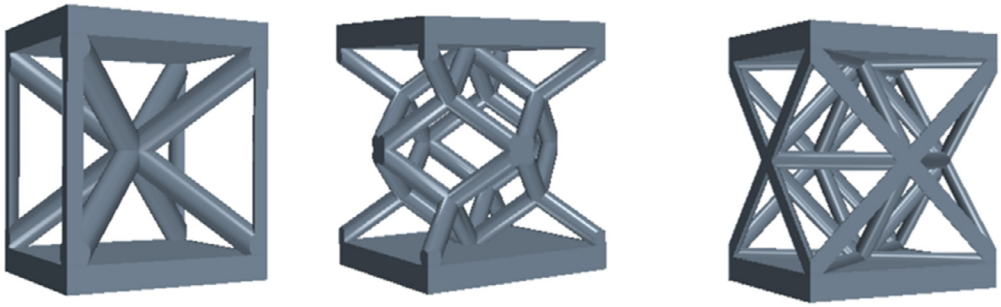

Fig. 1. Elementary unit cells drawing: (a) Bccz model; (b) Rhombic model; (c) Octet model.

timal designs and assessing the significance of various factors influencing the performance of the anti-icing system [17], [18].

2. Material and methods

In this study, Selective Laser Melting (SLM) [19] technique is employed to fabricate complex geometries, such as trabecular structures, with relatively high precision in a single component, eliminating the need for welds or joints [20]. SLM allows for seamless connections between different components without resorting to welding, bonding, riveting, or bolting processes. However, to meet the assembly tolerances, careful finishing of the interfaces is required due to manufacturing tolerances. Although the literature contains extensive research on the application of trabecular structures in various contexts [11], [21–25] there is limited focus on heat transfer considerations involving hot air mass passing through the plate that heats up external skins.

This work seeks to contribute by investigating the application of trabecular structures in designing a plate for an anti-icing system. The first case study examining the applicability of trabecular structures in heat exchangers was conducted by [26]. Several types of trabecular structures that can be fabricated using Additive Manufacturing (AM) technology have been studied and designed. Following a discussion of the capabilities and economic potential of the SLM technology used in creating the initial prototype plate for the integrated anti-icing system [27], subsequent sections will detail the selection of trabecular structures, the materials utilized, the Computational Fluid Dynamics (CFD) analysis model, and the specific approach to the statistical study.

In comparison to the currently available solutions that do not leverage Selective Laser Melting (SLM) manufacturing techniques combined with lattice structure designs traditional anti-icing methods often exhibit limitations in efficiency and sustainability, as they are characterized by higher weight, increased energy consumption, and non-optimized resource usage, all of which stand contrary to the goals of sustainable aviation [28–30]. This study marks a significant leap capitalizing on the distinctive properties of lattice structures and the unique capabilities of SLM manufacturing techniques to produce a single piece component without need of joint, rivets or welding.

2.1. Evaluated trabecular structures description

This study investigates three different types of trabecular structures used for constructing sandwich panels cores as single components, aiming to contribute to the field of anti-icing systems.

- BCCZ - Body-Centered Cubic with vertical struts along the Z-axis cell (Fig. 1a). This structure is the simplest and most feasible option, offering good mechanical properties even at low densities, both in terms of specific elastic modulus and strength. It also requires the least computational load and processing time in CAD and CAM compared to the other structures [31].
- ROMBIC - Rhombic Dodecahedron (Fig. 1b). This cellular structure minimizes the effects of instability on the internal struts, as beams deformed by bending exhibit both tensile and compressive stresses. The structure displays excellent fatigue strength characteristics [32].
- OCTET - The octet lattice configuration (Fig. 1c) provides a nearly isotropic elastic response. It comprises a unit cell composed of two Platonic solids: the tetrahedron and the octahedron. This lattice configuration yields exceptionally high specific energy absorption, a constant plateau stress between initial yield and densification, and a plastic Poisson ratio of zero [33].

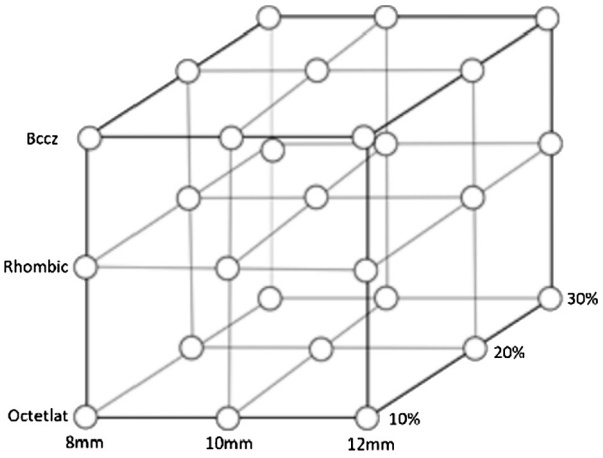

Fig. 2. DOE graphical overview.

The chosen material for the SLM additive manufacturing process is AlSi10Mg [34]. Furthermore, variations in individual cell sizes were carried out for each type of trabecular structure, defining the plate and each configuration of cell size for the three-trabecular breaks, with a variation in relative cell density of 10%, 20%, and 30%. Table 1 reports dimensions and relative density values adopted while Fig. 2 evidences the DOE approach used. Dimensions have been computed using Solidworks CAD and an iterative method.

Analyses were performed for each cell size and relative density of the structure. The proper design of the sandwich panel core should enable it to withstand normal aerodynamic load pressure during flight, reducing masses and improving mechanical performance [31].

Table 1
Table of cell size and relative density.

Cell Type	Cell Size [mm]	Relative Density [%]	Diameter of trabeculae rods [mm]	Wet surface [mm^2]
Rhombic	8	10	$5.71 \cdot 10^{-01}$	$3.07 \cdot 10^2$
		20	$8.07 \cdot 10^{-01}$	$3.44 \cdot 10^2$
		30	1.02	$3.66 \cdot 10^2$
	10	10	$7.50 \cdot 10^{-01}$	$4.82 \cdot 10^2$
		20	1.00	$5.36 \cdot 10^2$
		30	1.30	$5.74 \cdot 10^2$
	12	10	$8.00 \cdot 10^{-01}$	$6.63 \cdot 10^2$
		20	1.20	$7.72 \cdot 10^2$
		30	1.50	$8.20 \cdot 10^2$
Bccz	8	10	$4.00 \cdot 10^{-01}$	$3.50 \cdot 10^2$
		20	$6.00 \cdot 10^{-01}$	$4.12 \cdot 10^2$
		30	$7.50 \cdot 10^{-01}$	$4.40 \cdot 10^2$
	10	10	$5.00 \cdot 10^{-01}$	$5.49 \cdot 10^2$
		20	$7.50 \cdot 10^{-01}$	$6.42 \cdot 10^2$
		30	1.00	$6.96 \cdot 10^2$
	12	10	$6.00 \cdot 10^{-01}$	$7.80 \cdot 10^2$
		20	$9.50 \cdot 10^{-01}$	$9.43 \cdot 10^{-04}$
		30	1.20	$1.00 \cdot 10^2$
Octet	8	10	$3.50 \cdot 10^{-01}$	$3.70 \cdot 10^2$
		20	$5.50 \cdot 10^{-01}$	$4.09 \cdot 10^2$
		30	$7.00 \cdot 10^{-01}$	$4.42 \cdot 10^2$
	10	10	$5.00 \cdot 10^{-01}$	$5.65 \cdot 10^2$
		20	$7.00 \cdot 10^{-01}$	$6.48 \cdot 10^2$
		30	$8.50 \cdot 10^{-01}$	$6.87 \cdot 10^2$
	12	10	$5.50 \cdot 10^{-01}$	$7.82 \cdot 10^2$
		20	$8.00 \cdot 10^{-01}$	$9.17 \cdot 10^2$
		30	1.00	$9.84 \cdot 10^2$

Fig. 3 presents three graphs that elucidate the relationships between cell size, cell type, wet area, and relative density within the context of various trabecular structures. The critical observations derived from these graphs can be summarized as follows: First, a distinct linear trend is evident between cell size and wet area for all cell types. This finding is crucial for understanding the heat exchange performance and optimizing the design of trabecular structures for the intended anti-icing application. Second, a macroscopic comparability exists between the wet surfaces of different cell types with the same cell size. A comparative analysis of the three graphs reveals that values for distinct cell types are highly comparable when their cell sizes are the same. Lastly, a non-linear relationship is identified between relative density and wet surface. The graphs illustrate an inverse square-proportional trend, wherein the rate of wet surface area growth decreases as the radius of the beams increases. This observation highlights the importance of thoroughly considering the relationship between relative density and surface area when designing trabecular structures for anti-icing systems. Understanding this non-linear relationship is essential for optimizing the performance of the structures while minimizing the overall mass of the components.

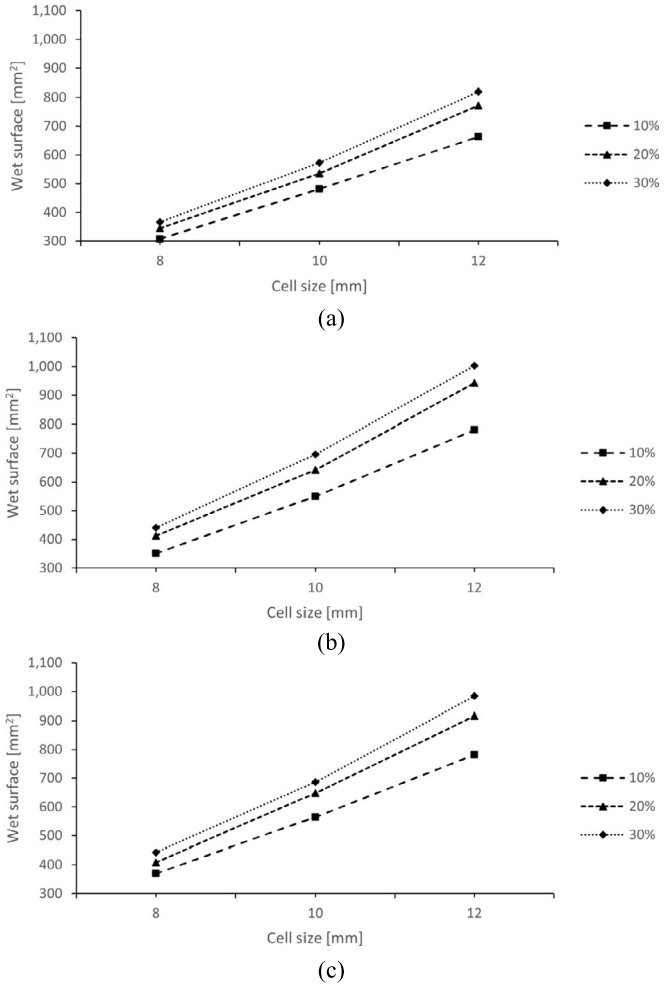

Fig. 3. Wet Surface vs Cell Size: (a) Bccz Cells, (b) Rhombic Cells, (c) Octet Cells.

2.2. CFD analysis

The evaluation of the heat transfer properties of the panel was conducted using a computational method based on Computational Fluid Dynamics (CFD) analysis, employing the commercial software STAR-CCM+. The process involved pre-processing (model preparation, interface setting, and control input conditions), execution (model resolution and real-time residue monitoring) within a single simulation environment, and post-processing through the extraction of relevant data. The chosen approach relied on finite volumes to address a conjugate fluid-solid heat transfer problem [35]. Starting from the fundamental equations governing motion (mass balance, energy, and momentum), STAR-CCM+ performs a partition on discrete subdomains, followed by a local discretization to obtain a set of algebraic equations from the initial partial

derivative equation (PDE). To account for turbulent phenomena, the equations were applied in the Reynolds-averaged form, introducing a new term in the momentum equilibrium equation.

$$\frac{\partial\left(\rho\overline{V}\right)}{\partial t}+\nabla\cdot\left(\rho\overline{V}\times\overline{V}\right)=-\nabla\cdot\overline{p}I+\nabla\cdot\left(T+T_b\right)+f_b \tag{1}$$

In the Equation (1) ρ represent the density V is the medium velocity, p is the medium pressure, T is the tensor of viscous stresses, I is the identity tensor, f_b is the resultant of the applied body forces and T_b is the additional term due to turbulence. This additional tensor depends on a series of unknowns that require a simplified model to be closed. The eddy viscosity model was employed, considering the analogy between molecular diffusion and turbulent processes. The introduction of this concept allowed for the modeling of additional unknowns. The classic form of Eddy viscosity is reported in Equation (2):

$$\mu_t=\rho C_\mu\frac{k^2}{\varepsilon} \tag{2}$$

In this equation it has been used a $k-\varepsilon$. Eddy viscosity results in fact, require two models that resolves two additional transport equations for the turbulent kinetic energy calculation k and for turbulent dissipation ε.

An alternative approach not used in this study involves a specific turbulent dissipation instead of the simile one. Once the eddy viscosity is determined, the Boussinesq's approximation of Reynolds tensor, T_b: can be calculated.

$$T_b=2\mu_t S-\frac{2}{3}\left(\mu_t\nabla\cdot\overline{V}\right)\overline{I} \tag{3}$$

Where S represents an average strain rate tensor given by:

$$S=\frac{1}{2}\left(\nabla\overline{V}+\nabla\overline{V^T}\right) \tag{4}$$

Regarding the energy balance and the heat transfer between two bodies, STAR CCM+ implements the equation in the following integral form:

$$\begin{aligned}&\frac{\partial}{\partial t}\int_V\rho E dV+\oint_A\rho HV\cdot da\\&=-\oint_A\dot{q}\cdot da+\oint_A T\cdot Vda+\int_V f_b\cdot VdV+\int_V S_u dV\end{aligned} \tag{5}$$

In the Equation (5) E represent the energy total system, H the total enthalpy, $\dot{q}$ is the vector heat flow, T is the viscous stress tensor, V is the velocity vector and f_b is the force vector. S_u is instead a term that combines the contribution of different sources of internal energy such as radiation, chemical reactions etc. The implemented model resolves all balance equations separately in each domain, except for enthalpy. This equation is coupled with the fluid Reynolds-Averaged Navier-Stokes (RANS) equations. In Conjugate Heat Transfer (CHT), the enthalpy equation is solved considering both fluid and solid domains, with coupling at the interfaces identified by the meshing process.

2.3. Physics modeling

In this study, the adopted fluid dynamic model simulates the conditions of the experimental bench outlined in the referenced thesis document [36]. The simulation's underlying physics focus on the turbulent heat transfer of hot air as it passes through the trabecular core of the panel. During this process, the warm air transfers heat to the rods of the trabeculae, which in turn transport it via conduction to the external surface of the sandwich panel [8].

Table 2
Air and aluminium model.

Air Continua	Model
Space	Three Dimensional
Time	Steady
Material	Gas
Flow	Segregated Flow
Gradient Metrics	Gradients
Equation of State	Constant Density
Energy	Segregated Fluid Temperature
Optional Model	Cell Quality Remediation
Viscous Regime	Turbulent
Turbulence	Reynolds-Averaged-Navier-Stokes
Reynolds-Averaged Turbulence	K-Epsilon Turbulence
Wall Distance	Exact Wall Distance
K-Epsilon Turbulence Model	Realizable K-Epsilon Two-Layer
	Two-Layer All y + Wall Treatment
Aluminum Continua	**Model**
Space	Three Dimensional
Time	Steady
Material	Solid
Gradient Metrics	Gradients
Equation of State	Constant Density
Energy	Segregated Solid Energy
Optional Model	Cell Quality Remediation
Option Model	Radiation
Radiation	Participating Media Radiation (DOM)
Radiation Spectrum (Participating)	Gray Thermal Radiation

Table 3
Air and aluminium data.

Air Continua	Method	Value
Density Constant	Constant	1.18415 kg/m^3
Dynamic Viscosity	Constant	1.855 · 10-5 Pa·s
Specific Heat	Constant	1003.62 J/kg·K
Thermal Conductivity Constant	Constant	0.026 W/m·K
Turbulent Prandtl Number	Constant	0.9
Aluminum Continua	**Method**	**Value**
Density	Constant	2702.0 kg/m^3
Specific Heat	Constant	940 J/kg·K
Thermal Conductivity	Constant	170.96 W/m·K
Scattering Coefficient	Constant	0.03/m
Absorption Coefficient	Constant	0.05/m
Air Continua	Method	Value

Table 4
Boundary conditions reference value.

Air Inlet		
Physics Value	Methods	Value
Mass flow rate	Constant	0.002072 kg/s
Total temperature	Constant	75 °C
Air Outlet		
Physics Value	Methods	Value
Pressure	Constant	1.42 bar
Static Temperature	Constant	20 °C

Considering the standard laboratory conditions, there is natural convection outside the panel with an ambient temperature of 20 °C. These conditions are accounted for in accordance with the experimental campaign detailed in the doctoral thesis [36]. Table 2 reports the model selected while Table 3 outlines the reference data used.

Boundary conditions for air part have been settled up are mass flow inlet with specified Mass flow rate and Total Temperature and Pressure outlet. Reference data are reported in Table 4.

Regarding the aluminum material in the model, not exposed part interfaces were configured as adiabatic walls, with the ex-

Table 5
Physical value of the aluminium alloy.

Physics Value	Methods	Value
Heat Transfer Coefficient	Constant	14.85 W/m^2·K
Ambient temperature	Constant	20 °C
Surface emissivity	Constant	0.46

ception of interfaces air-solid involving indoor air and the natural convection top and bottom surfaces in contact with outdoor air. At the first interface, heat is transferred from the warm internal heating air to the aluminum, while at the second interface, heat transfer occurs both within the aluminum and through convective heat exchange with the laboratory environment. This setup ensures an accurate representation of the heat transfer processes in the simulation.

In this study, the external natural convection coefficient h was determined using the methodology outlined in [37]. Initially, the characteristic length (L) was set at 0.01 m, followed by assigning the maximum achievable temperature coefficient T_s to 150 °C. By utilizing these values, the Grashof number was subsequently calculated through the designated formula:

$$Gr = \frac{g\beta\,(T_s - T_\infty)\,\rho^2 L^3}{\mu^2} \tag{6}$$

The value obtained is equal to 18.9–103. This value is less than 107 therefore, being a natural convection, it is possible to formulate the Nusselt number as:

$$Nu = 0.54 \cdot (Pr \cdot Gr)^{\frac{1}{4}} \tag{7}$$

Obtaining a value of 5.8. Finally, the convective coefficient was calculated according to equation (8) as:

$$h = Nu\frac{k}{L} = \backslash SI 14.85\ \mathrm{W/m^2\,K} \tag{8}$$

Upon determining the convective heat transfer coefficient, all the relevant physical data pertaining to continuous aluminum can be incorporated, as shown in Table 5. Given that this analysis is steady-state, there is no need to specify a computational time step. Simulation setup, since it is devoted to evaluate regime parameters has been imposed implicit. Rather, a maximum number of iterations (5000) was selected to achieve an acceptable level of convergence. The analyses were conducted using the Polito High-Performance Computing Cluster, which is based on the Linux Kernel.

2.4. Model setup

A sandwich panel of 4x4 cells has been setup for the present analysis. The general overview of the model is reported in Fig. 4. The two physical models, the trabecular structure and the internal air portion of the panel through which the hot air flow will pass, are perfectly superimposed, which is essential for the CHT simulations. After transferring the created CAD model to the CAE solver, the appropriate surfaces were separated to impose the necessary boundary conditions for solving the problem. Subsequently a non-structured mesh has been applied to the models, as reported by Fig. 5.

Automated Part-Based Meshing (PBM) operations have been adopted, separating meshing from the physics, ensuring flexibility and repeatability. PBM manages meshers, default controls, and custom controls while enabling Parallel Meshing execution for faster volume mesh generation and compatibility with HPC© clusters. Surface remesher, automatic surface repair tool, polyhedral mesher, and prism layer mesher were employed for mesh generation. Polyhedral cells are particularly suitable for heat transfer, swirling flows, and complex flow analyses. Prism layer mesher is essential for cases involving conjugate heat transfers and turbulent flow fields, as it resolves velocity and temperature gradients normal to the wall accurately. Custom control parameters were chosen as shown in Table 6. Those parameters, evaluated after an extensive mesh study, have been maintained for all the simulations.

Table 6
Meshing models custom controls.

Mesh Controls	Values
Base Size [mm]	0.8
Surface Growth Rate	1.5
Auto Repair Min Proximity	0.01
Number of Prism Layer	5
Prism Layer Near Wall Thickness [mm]	0.0236
Prism Layer Total Thickness	30% of Base size
Mesh Grow Factor	1.75
Number of Aluminum (example)	∼6252780
Number of Cells Air Continua (example)	∼7062361

3. Results

The following sections will present the results obtained from the fluid-dynamic tests and provide an analysis of the trends and data necessary for drawing conclusions.

The analysis was conducted sequentially, starting with the cells featuring the BCCZ trabecular structure, followed by Rhombic, and finally Octet. The simulation results are presented in the same order, allowing for a structured and systematic examination of the various configurations and their performance in the context of the anti-icing panel.

3.1. CFD analysis results

The CFD analysis carried out were iterated for 500 steps each. The residual graph shown as example in Fig. 6 evidences a global stability of the numerical process and a residual value well below 0.1 for all the errors computations.

All the 27 runs performed with the same trend. The second graph reported in Fig. 6b report the total energy error vs iteration trend showing a pass through the imposed threshold of 0.01 and a monotonic decreasing trend.

Appendix A Contour Plot discloses for each case contours plot of plate temperature, flow temperature, static pressure and flow velocity. For assessing heat transfer performance, the critical parameters of interest are Pressure Drop, Heat Transfer Interaction, and Temperature Drop. These parameters are vital for characterizing the behavior of various trabecular structures as hot air flows through them. The analysis focuses on determining the pressure needed to maintain a specific flow uniformity within the plate and identifying which configurations exhibit the highest heat transfer efficiency. In addition to pressure variations across the heat transfer interface, the capacity of the structure to absorb heat under the specified conditions is also assessed. Furthermore, the temperature difference between the inlet and outlet of the airflow is crucial for pinpointing the configuration with the most substantial heat loss based on the structure and its size. The gathered data were subjected to statistical analysis using Design of Experiment (DOE) techniques. Subsequently, the findings will be compared, insights will be drawn from the performed analyses, and observations will be evaluated for potential application in future scenarios and contexts. Data extrapolated are reported in Table 7 and detail statistical analysis is presented for each cell size.

3.2. Bccz cells DoE analysis

The analysis of the graphs reported in Fig. 7 reveals critical insights into the relationship between cell size, relative density, and

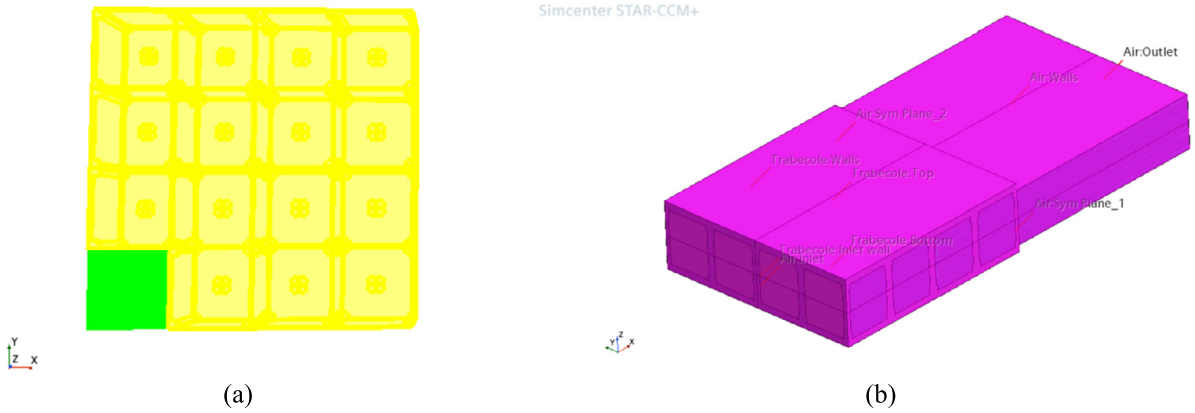

Fig. 4. Model Setup overview: (a) vertical view, (b) isometric view of the test panel.

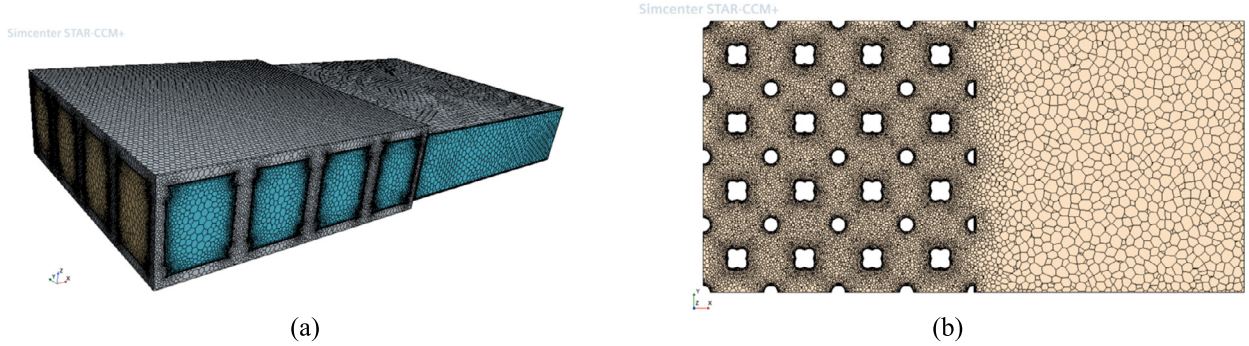

Fig. 5. Mesh view: (a) isometric, (b) cross section.

Table 7
CFD Data Evaluated.

Cell Type	Cell Size	Relative Density	Pressure Drop [bar]	Heat Transfer Interface [W]	Temperature Drop [°C]
Rhombic	8	10	$1.7483 \cdot 10^{-03}$	8.4169	3.9341
		20	$3.7167 \cdot 10^{-03}$	8.7046	3.9008
		30	$7.1782 \cdot 10^{-03}$	9.0448	3.7765
	10	10	$8.2101 \cdot 10^{-04}$	11.2678	5.3873
		20	$1.5425 \cdot 10^{-03}$	12.0376	5.6883
		30	$3.2396 \cdot 10^{-03}$	12.7767	5.9038
	12	10	$3.3201 \cdot 10^{-04}$	13.4033	6.4543
		20	$7.6401 \cdot 10^{-04}$	15.0825	7.2173
		30	$1.4127 \cdot 10^{-03}$	16.1452	7.6763
Bccz	8	10	$2.0986 \cdot 10^{-03}$	6.5229	2.9979
		20	$5.3361 \cdot 10^{-03}$	11.1724	4.9902
		30	$1.0838 \cdot 10^{-02}$	10.8180	4.3503
	10	10	$8.940 \cdot 10^{-04}$	13.7421	6.5952
		20	$2.2437 \cdot 10^{-03}$	15.0143	7.0860
		30	$5.8326 \cdot 10^{-03}$	15.8187	7.1804
	12	10	$4.4601 \cdot 10^{-04}$	17.0058	8.2013
		20	$1.2945 \cdot 10^{-03}$	18.9848	9.0868
		30	$2.8569 \cdot 10^{-03}$	20.2589	9.5585
Octet	8	10	$2.2567 \cdot 10^{-03}$	10.3325	4.8572
		20	$5.2178 \cdot 10^{-03}$	12.5458	5.7024
		30	$1.0026 \cdot 10^{-02}$	12.0391	5.0506
	10	10	$1.1912 \cdot 10^{-03}$	15.6206	7.4672
		20	$2.3505 \cdot 10^{-03}$	16.5303	7.8677
		30	$3.8202 \cdot 10^{-03}$	16.4311	7.6958
	12	10	$5.0821 \cdot 10^{-04}$	19.4975	9.1256
		20	$1.0375 \cdot 10^{-03}$	19.9719	9.5830
		30	$1.7730 \cdot 10^{-03}$	20.5422	9.8008

their impact on pressure drop, heat transfer, and temperature drop in lattice structures:

- Pressure Drop: The graphs demonstrate that an increase in cell size leads to a decrease in pressure drop, as larger cells facilitate more airflow to pass freely within the lattice. Conversely, a rise in relative density results in an increase in pressure drop, owing to the reduced dimensions of the passageways. The contour plot highlights a region of low-pressure drop that corresponds to low relative density and high cell size.

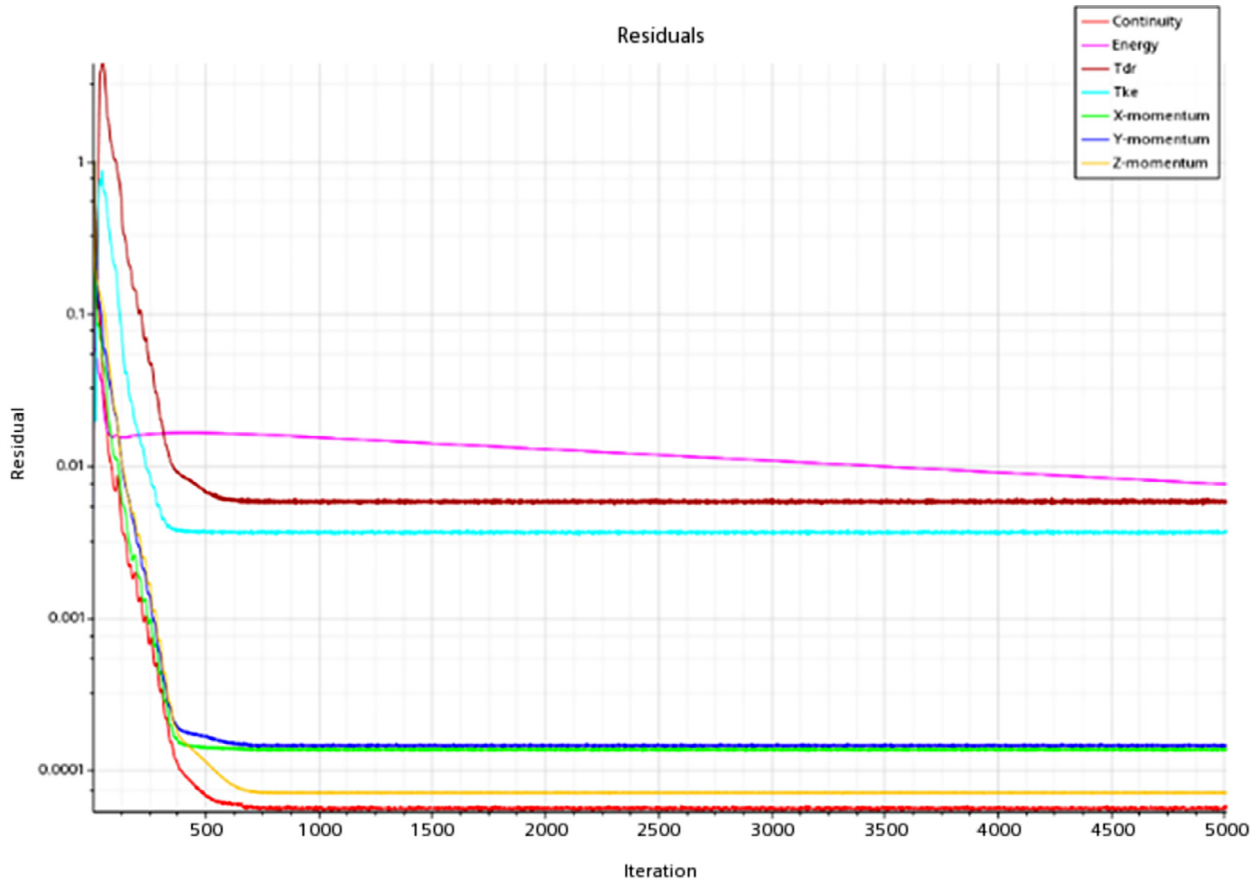

(a)

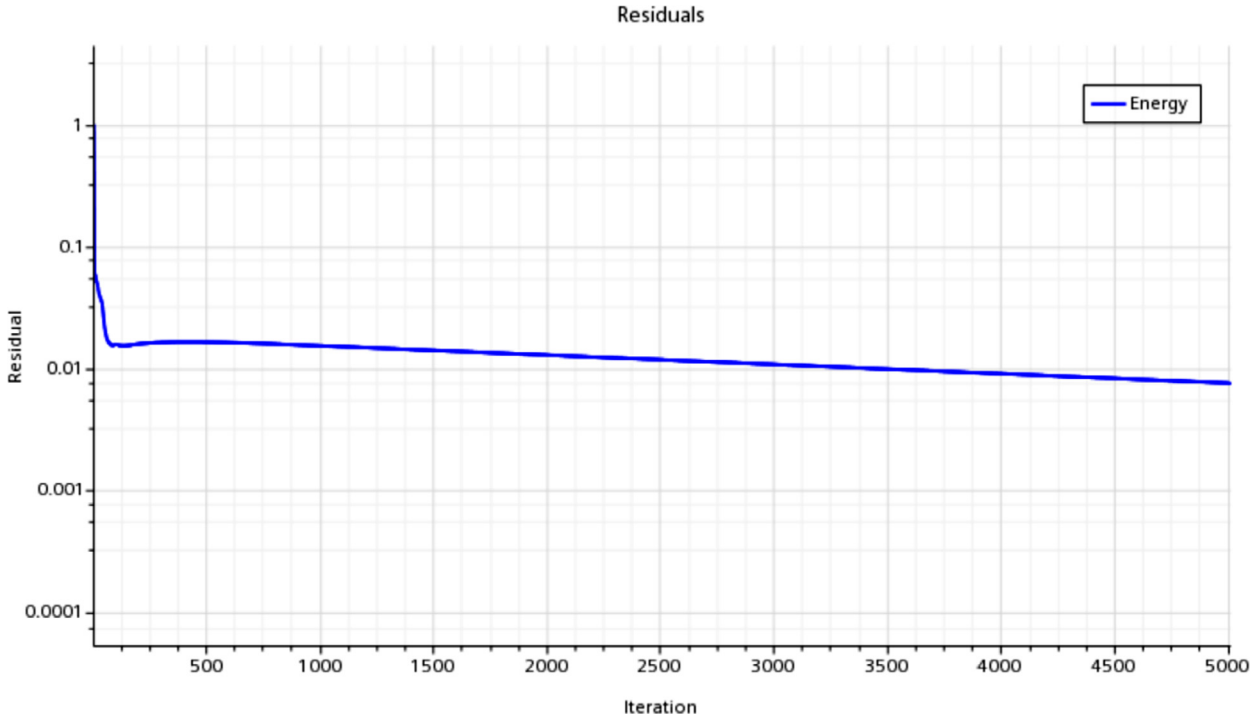

(b)

Fig. 6. Iteration trend: (a) Residual vs Iteration; (b) Energy error vs iteration.

- Heat Transfer: The graphs show that heat transfer increases with cell size, as the air moves more quickly through the structure. Heat transfer also increases, albeit at a slower rate, with relative density due to the expansion of the wet area. Therefore, the most promising area for efficient heat transfer lies in configurations with large cell sizes and high densities, although density plays a relatively minor role in this aspect.
- Temperature Drop: As anticipated, the temperature drop behaves similarly to heat transfer. However, the diminished effect of relative density on temperature drop is more apparent in this case. The primary influence on temperature drop stems from cell size, as indicated by the contour plot.

3.3. Rhombic cells DoE analysis

The examination of the graphs, reported in Fig. 8 underscores critical observations concerning the interplay between cell size, relative density, and their influence on pressure drop, heat transfer, and temperature drop in rhombic lattice configurations:

- Pressure Drop: The graphs demonstrate that enlarging cell size contributes to a decrease in pressure drop, paralleling the findings for the BCCZ lattice. Simultaneously, a rise in relative density provokes an escalation in pressure drop, with the pattern displaying a more pronounced quadratic characteristic. The contour plot identifies an area of minimal pressure drop associated with a combination of low relative density and elevated cell size.
- Heat Transfer: The increase in heat transfer corresponds to an increase in cell size, mirroring the observations made for the BCCZ lattice. The influence of relative density on heat transfer follows a square root pattern, leveling off once the relative density surpasses 20%. As a result, the most favorable region for effective heat transfer resides in configurations characterized by large cell sizes and elevated densities, although the density's contribution is marginal.
- Temperature Drop: As predicted, the temperature drop exhibits a similar trend to heat transfer. Nonetheless, the reduced impact of relative density is more pronounced in this instance, with negligible variation detected between 20 and 30% of relative density. The primary factor affecting temperature drop is the cell size, as illustrated by the contour plot.

3.4. Octet cells DoE analysis

The graphical analysis reported in Fig. 9 sheds light on the critical interactions between cell size, relative density, and their influence on pressure drop, heat transfer, and temperature drop within octet lattice structures:

- Pressure Drop: In line with observations in BCCZ and rhombic cells, a larger cell size corresponds to a reduced pressure drop. Concurrently, increasing relative density results in a higher pressure drop, exhibiting a trend akin to that of the rhombic cell configuration. The contour plot reveals a zone with minimal pressure drop, corresponding to low relative density and substantial cell size.
- Heat Transfer: As found in the BCCZ and rhombic cell structures, heat transfer is positively correlated with cell size. The impact of relative density on heat transfer follows a square root trajectory, reaching a plateau beyond 20% relative density. As a result, the ideal region for effective heat transfer lies within the configurations characterized by expansive cell sizes and elevated densities, although the role of density remains minimal.
- Temperature Drop: As expected, the temperature drop shares a similar pattern with heat transfer. However, the diminished influence of relative density becomes more pronounced, presenting a marginal decline beyond 20% relative density, which signifies the achievement of a local maximum temperature drop at this percentage. The primary determinant of temperature drop is the cell size, as evidenced by the contour plot.

3.5. Pressure drop analysis

Our investigation, graphically disclosed in Fig. 10 reveals that BCCZ cells exhibit the lower pressure drop among the three lattice structures considered, which also include rhombic and octet cells. The contrasting topologies of rhombic and octet cells, characterized by less preferential passageways and more intricate airflow patterns, contribute to their higher-pressure drops. Moreover, rhombic cells tend to have a greater pressure drop compared to octet cells. Across all three-cell types, the pressure drop displays a quadratic trend as a function of relative density, with an increase in pressure drop accompanying a rise in cell size. As illustrated in Fig. 10 data analysis reveals a quadratic relationship between pressure drop and relative density across all graphs, and a consistent trend, also quadratic in nature, indicates that smaller cell sizes are associated with higher pressure loss, regardless of cell type.

3.6. Temperature drop analysis

From Fig. 11 it is possible to observe that the temperature drop follows a square root trend with respect to cell size. An increase in both cell size and relative density results in a higher temperature drop. This trend is particularly evident in BCCZ cells, where the differences in temperature drop as a function of relative density increase are proportional to cell size. In other words, larger cell sizes demonstrate a more significant influence of relative density on temperature drop compared to smaller sizes. For the other two cell types, rhombic and octet, the trends are somewhat more intricate and less distinct. However, the overall shape of the trends across all specimens is predominantly consistent with a square root pattern. It is important to note that the temperature drop is lowest in BCCZ cells, followed by octet cells, with the highest temperature drop observed in rhombic cells. This observation highlights the complex interplay between cell size, relative density, and temperature drop in lattice structures, underscoring the importance of considering these factors when evaluating the thermal performance of such materials.

3.7. Heat transfer interface analysis

As illustrated in the subsequent graphs depicted in Fig. 12, a direct proportionality exists between temperature drop and heat transfer interface. The resulting curves, obtained through interpolation of the parameters, manifest as linear relationships.

By analyzing the correlation between the heat transfer interface trend and pressure drop values, it has been possible to obtain functioning maps (Fig. 13) that illustrate the behavior of the plates and their internal trabecular structures. The heat transfer measured through power transfer between fluid and structure highlights the properties existing between pressure and heat transfer, as described by Nusselt's law. Upon interpolating the data from the fluid-dynamic simulations, Fig. 13 reveals the map pertaining to the Bccz structure, which exhibits lower heat transfer interface values compared to the Rhombic and Octet structures.

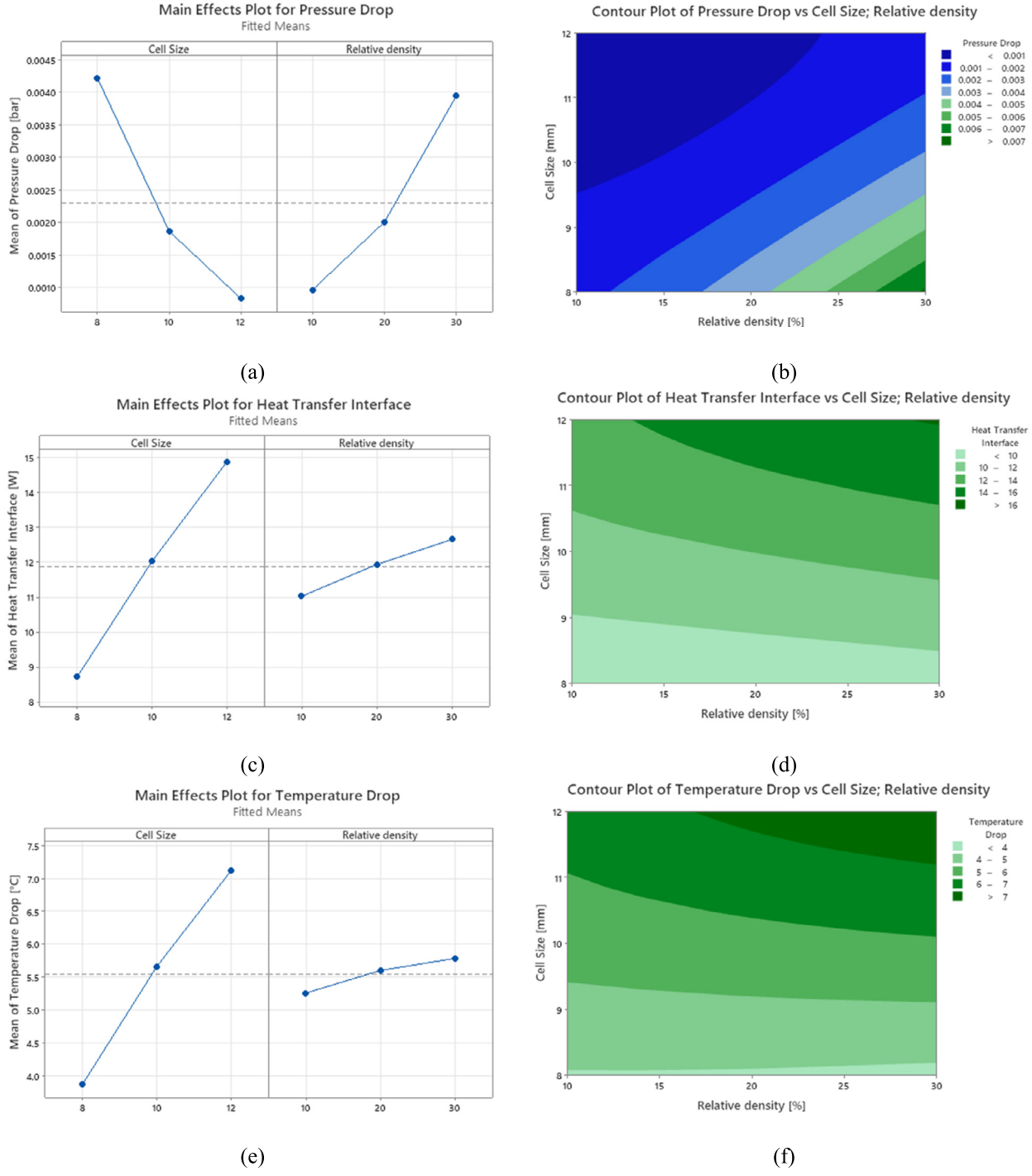

Fig. 7. Bccz DOE Cells Analysis: (a) Main Effect for Pressure Drop; (b) Contour Plot of Pressure Drop vs Cell size and Relative Density; (c) Main Effect for Heat Transfer Interface; (d) Contour Plot of Heat Transfer Interface vs Cell size and Relative Density; (e) Main Effect for Temperature Drop; (f) Contour Plot of Temperature Drop vs Cell size and Relative Density.

For the Bccz case shown in Fig. 13(a), the map indicates that by increasing the size and relative density for this type of structure within these parameters, there is an increase in Heat Transfer. The maximum heat transfer interface value of 16.1452 W is reached with a cell size of 12 mm, a density of 30%, and a pressure drop of 1.4127 x 10^{-03} bar.

For Rhombic and Octet structures in Fig. 13(b) and (c), they exhibit higher heat transfer interface values than the Bccz case. These structures display trends leading to a decrease in heat transfer interface when a certain pressure drop value is attained. Specifically, for a cell size of 8 mm in both Rombic and Octet structures, the curve trend reaches a maximum and then declines once a relative cell density of 30% is achieved. This is primarily attributed to their topology, wherein an increase in relative density creates challenges for the hot fluid to pass through, leading the plate to exhibit characteristics akin to a porous plate.

The Octet structure is particularly noteworthy, as it presents a more stringent limit on relative density for a cell size of 8 mm. Indeed, even before reaching a relative density of 30%, the structure begins to lose efficiency in heat exchange. However, when increasing cell size, the situation improves, as previously stated in the DOE study, with the highest exchanges obtained for cells

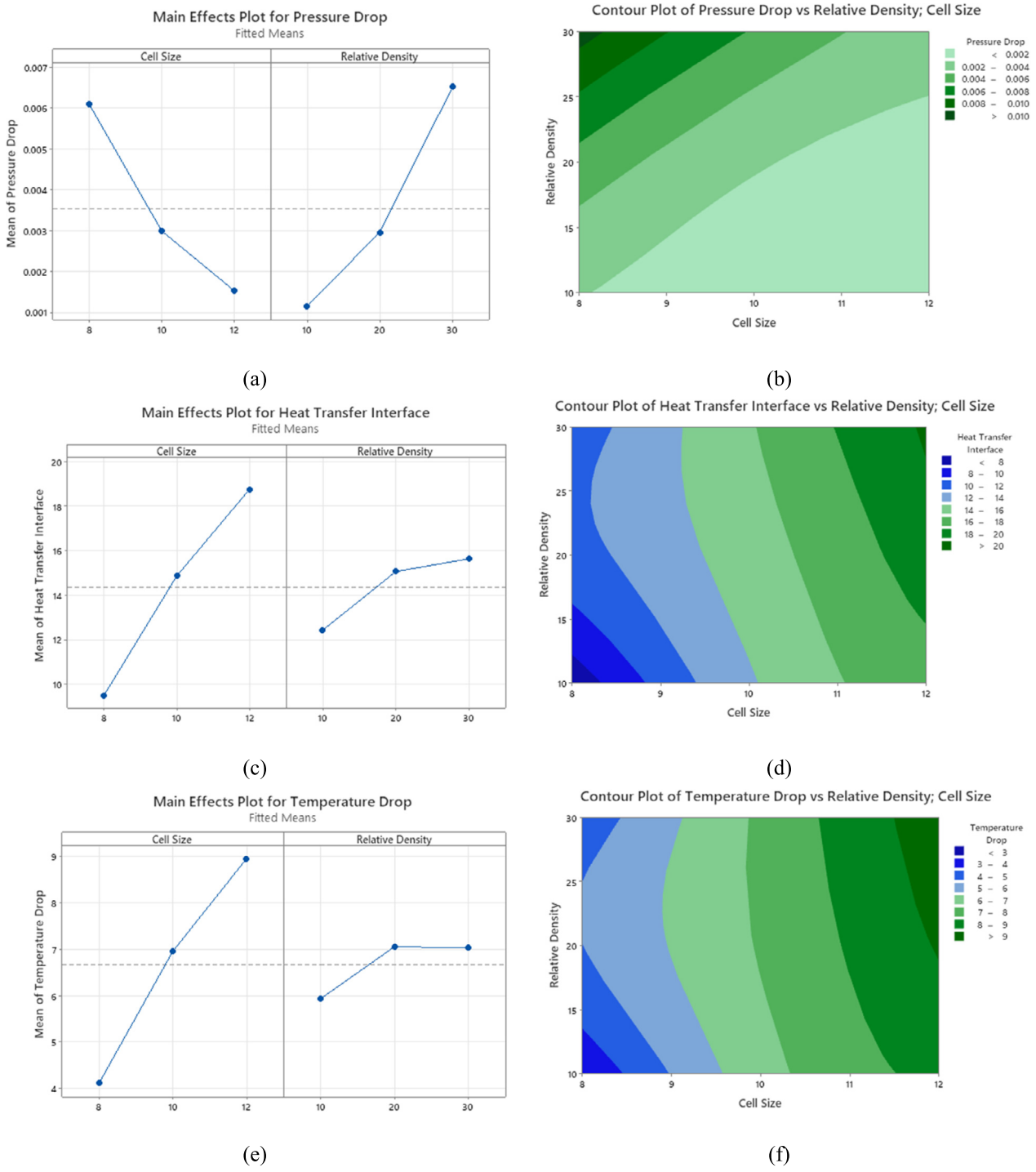

Fig. 8. Rhombic DOE Cells Analysis: (a) Main Effect for Pressure Drop; (b) Contour Plot of Pressure Drop vs Cell size and Relative Density; (c) Main Effect for Heat Transfer Interface; (d) Contour Plot of Heat Transfer Interface vs Cell size and Relative Density; (e) Main Effect for Temperature Drop; (f) Contour Plot of Temperature Drop vs Cell size and Relative Density.

with a cell size of 12 mm and $\varepsilon = 30\%$. The maximum heat transfer interface value of 20.54 W is achieved by the Octet structure. Dimensionally, all parameters between Rhombic and Octet are comparable and similar, except for the pressure drop in the octet case, which has slightly lower values than in the rhombic case.

In conclusion, the maps serve to define the operating points of the plates and their related trabecular structures, predict behaviors, and identify points with maximum heat exchange efficiency. They also anticipate the points in relation between the heat transfer interface and pressure drop, where the structures behave as porous structures, decreasing efficiency.

4. Conclusions

In conclusion, the conducted simulations and data analysis have established a model for the behavior of additive manufactured plates, which takes advantage of the ease of producing complex shapes and creating increasingly efficient integrated systems. In the case of the examined panel, the heat transfer capabilities of

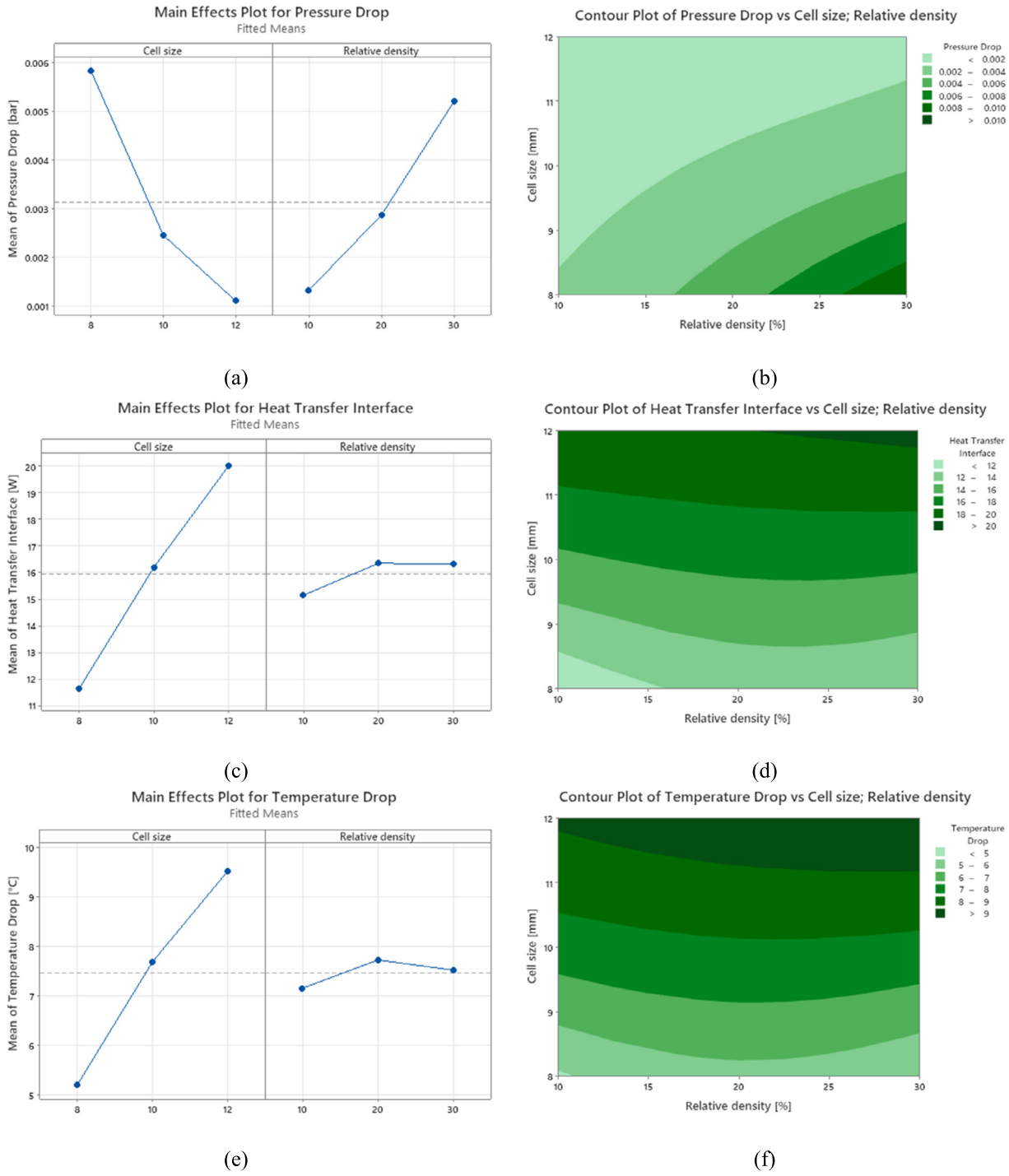

Fig. 9. Octet DOE Cells Analysis: (a) Main Effect for Pressure Drop; (b) Contour Plot of Pressure Drop vs Cell size and Relative Density; (c) Main Effect for Heat Transfer Interface; (d) Contour Plot of Heat Transfer Interface vs Cell size and Relative Density; (e) Main Effect for Temperature Drop; (f) Contour Plot of Temperature Drop vs Cell size and Relative Density.

AlSi10Mg through the properties of trabecular cells enable the production of panels that are not only damage-resistant but also demonstrate heat-transfer capabilities [27]. It is important to emphasize the potential of using this technology for realizing integrated wing systems for UAVs and other aircraft, creating air intake lips subjected to ice formation like wings, or even developing future heat transfer systems for liquid propellant rocket nozzles.

The evidenced thermal exchange behavior, analyzed through CFD simulations using STAR CCM+ software, exhibits a notable increase in heat transfer with the rise in relative cell density. However, increasing the density also escalates the pressure drop between the inlet and outlet of the hot flow. The plate's performance varies depending on the trabecular structure, cell size, and relative density, particularly in the Rhombic and Octet cases, where heat transfer performance decreases as the relative density increases, transitioning from a trabecular structure to a plate with porous behavior.

The Rhombic and Octet cells exhibit the highest Heat Transfer Interface values but become less efficient above 25% relative density. Pressure drop values have a quadratic trend with respect

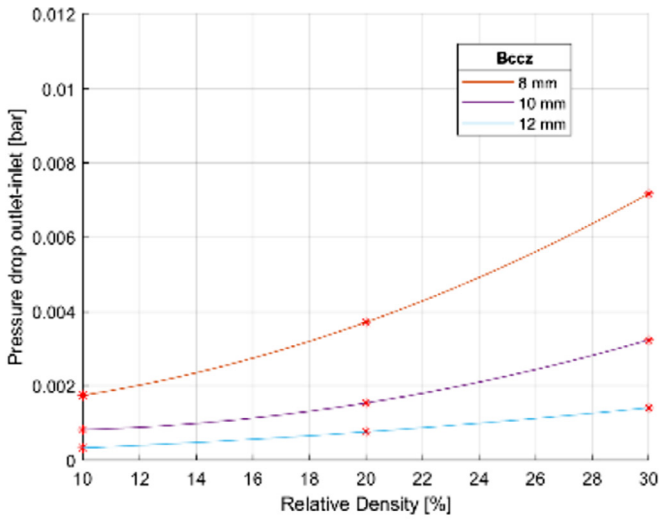

(a)

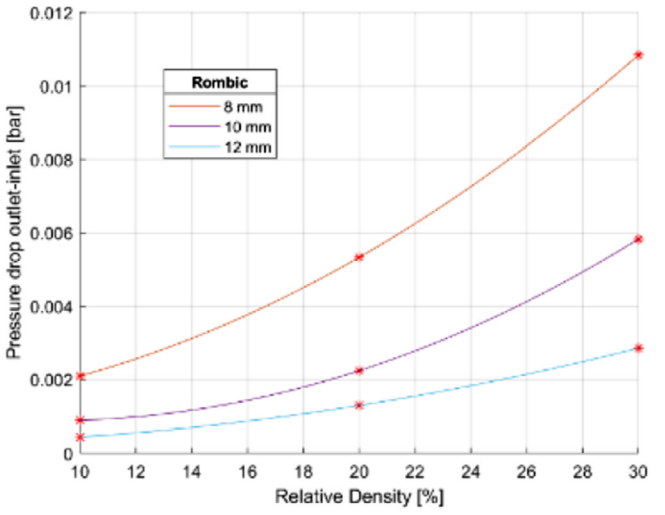

(b)

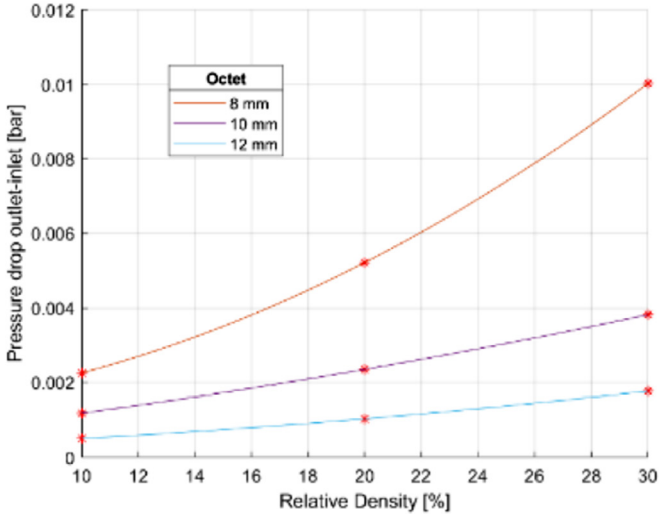

(c)

Fig. 10. Pressure Drop vs Relative Density: (a) Bccz Cells, (b) Rhombic Cells, (c) Octet cells.

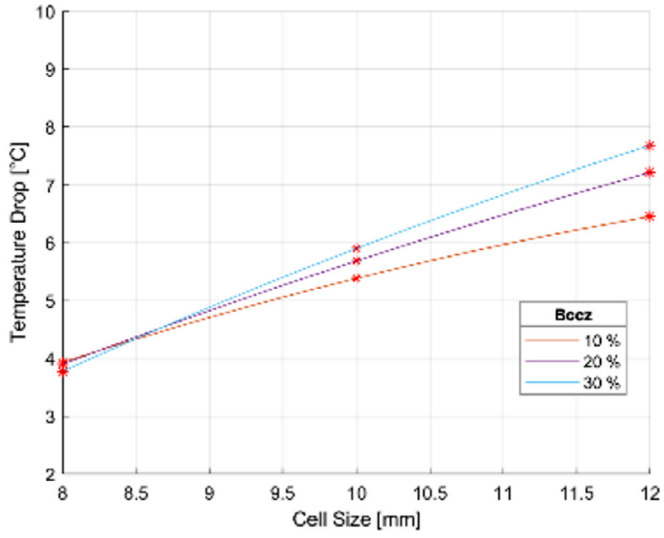

(a)

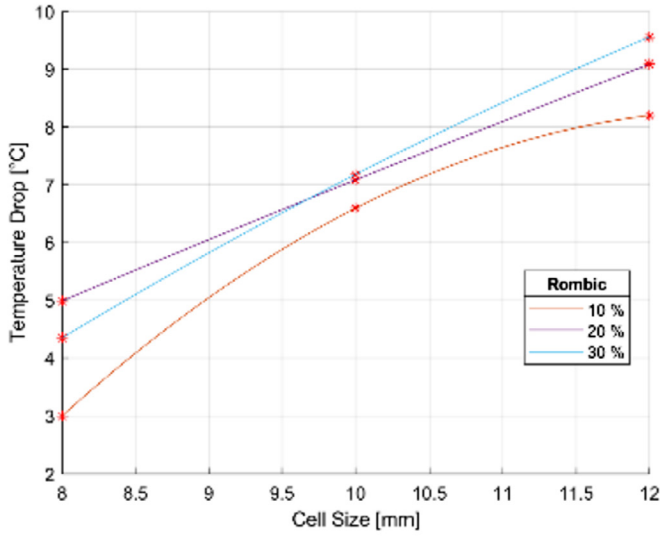

(b)

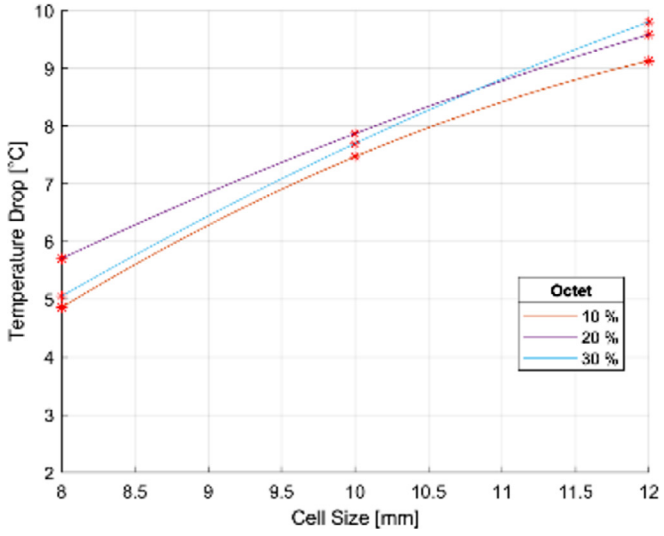

(c)

Fig. 11. Temperature Drop vs Cell size: (a) Bccz Cells, (b) Rhombic Cells, (c) Octet cells.

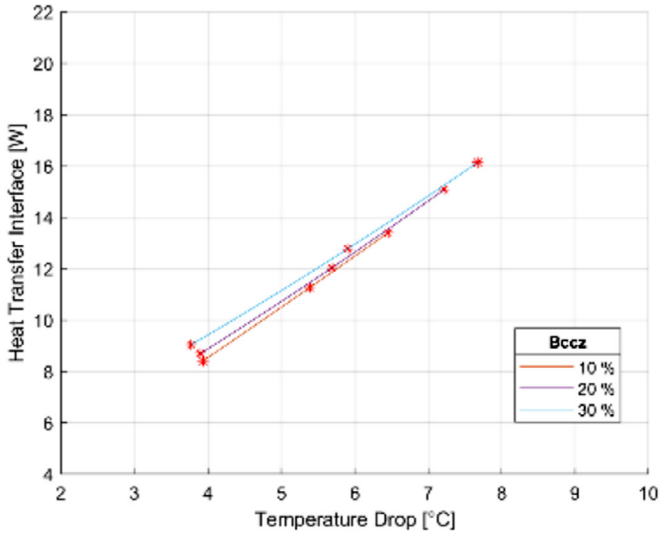

(a)

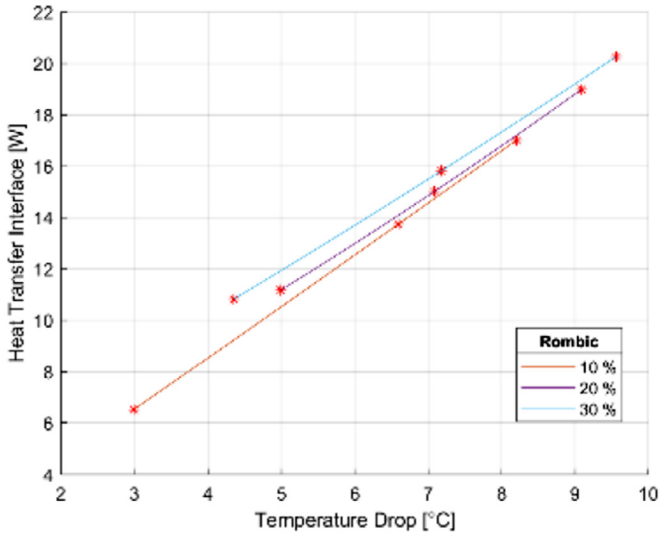

(b)

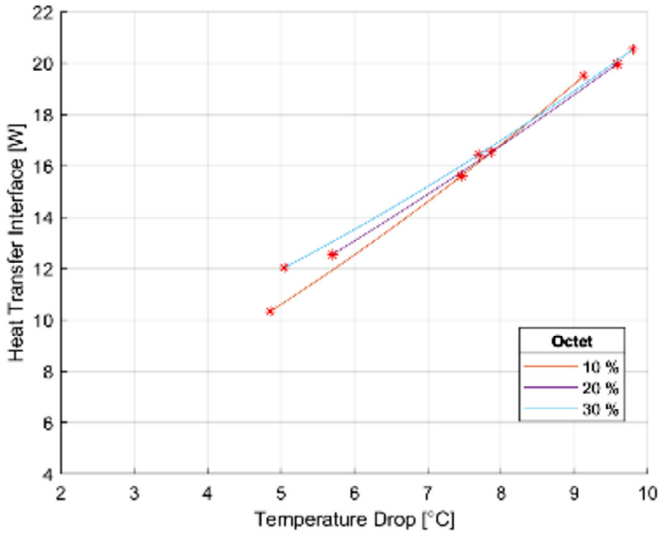

(c)

Fig. 12. Heat Transfer vs Temperature Drop: (a) Bccz Cells, (b) Rhombic Cells, (c) Octet cells.

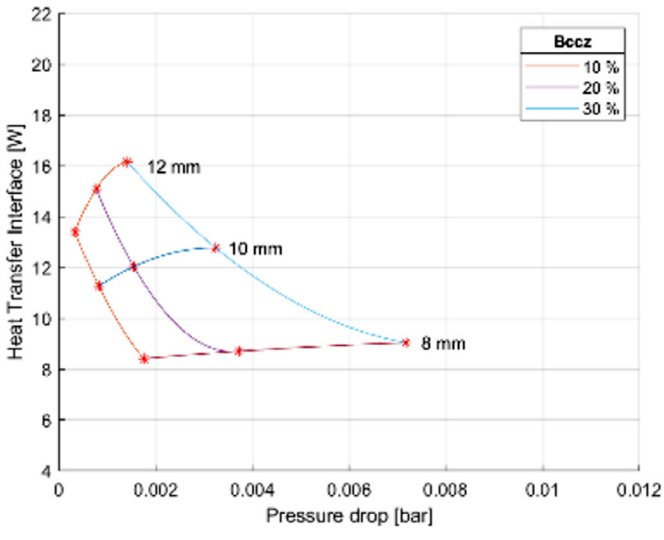

(a)

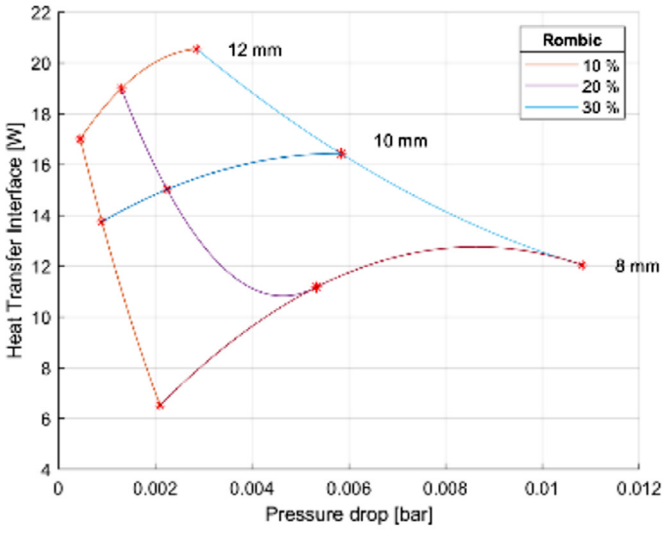

(b)

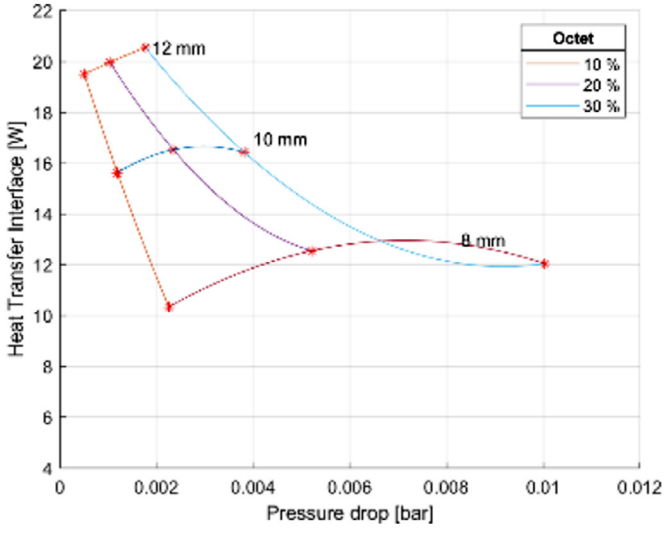

(c)

Fig. 13. Heat Transfer vs Pressure Drop: (a) Bccz Cells, (b) Rhombic Cells, (c) Octet cells.

to cell size, as the intercellular space increases with growing cell size, causing the parabolic curve to flatten out downwards. The plate with the highest heat transfer value is the Octet configuration with a 12 mm cell size and 30% relative density, equaling 20.54 W. The Temperature Drop demonstrates a fairly linear and proportional trend to the Heat Transfer Interface. Maps as the one reported in Fig. 13 provide to the readers interesting and valuable design outcome useful when tailoring a novel structure for different purposes. This is a first step towards the future works aimed to obtain an analytical comprehensive model that permit to design and tailor lattice structures for heat exchanger use.

Based on the provided data and observations, future studies could continue identifying the optimal cell size and relative density according to design needs, using the data presented here. Subsequent investigations may focus on experimentally testing various trabecular configurations and analyzing the correspondence between experimental and analytical results, ultimately determining the most suitable configurations based on the plate's function.

5. Appendix A Contour plot

5.1. Bccz

5.1.1. Cell size 8 mm

See Fig. 14.

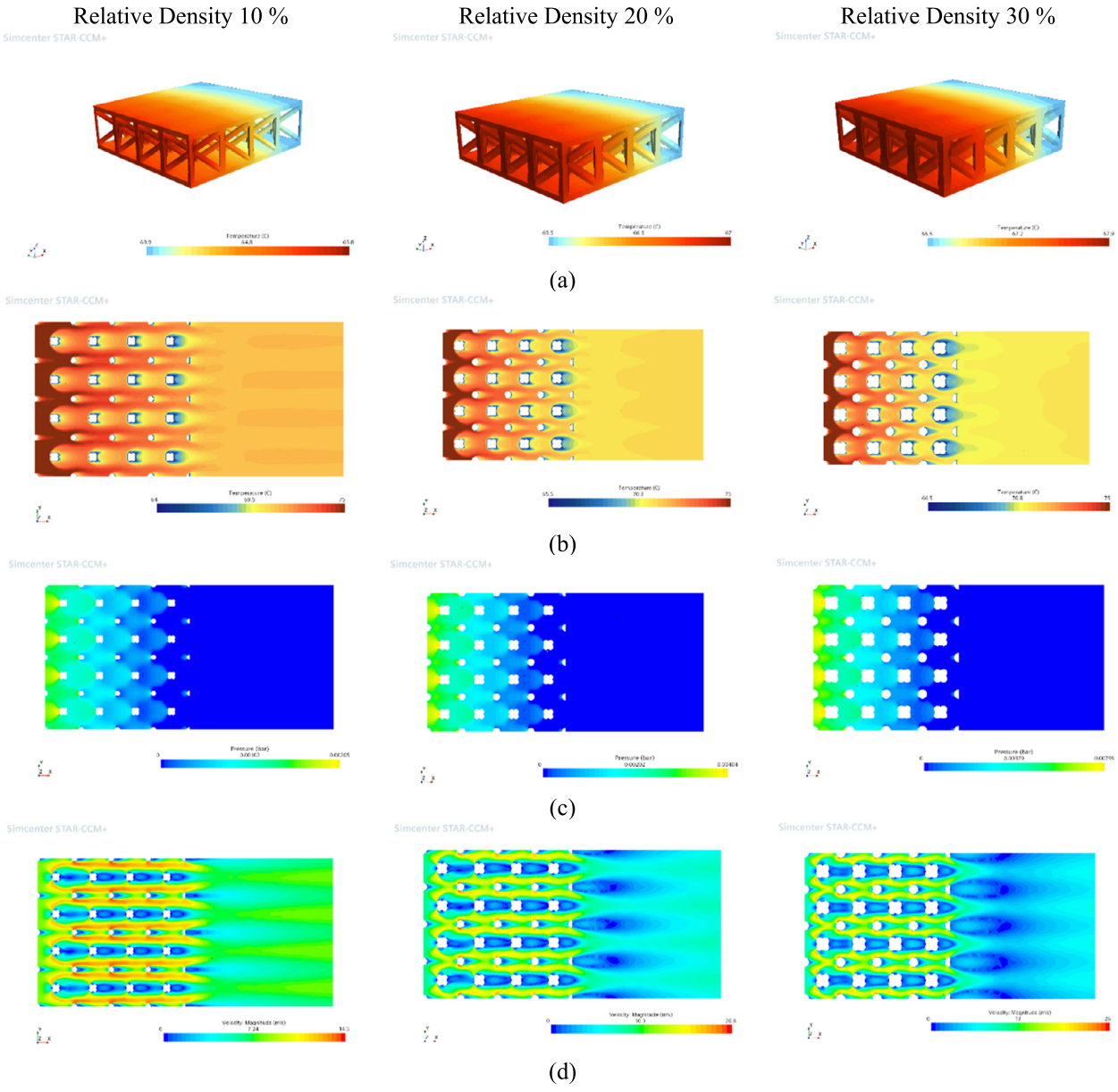

Fig. 14. Bccz 8 mm simulation: (a) plate temperature, (b) flow temperature, (c) static pressure, (d) flow velocity.

5.1.2. Cell size 10 mm

See Fig. 15.

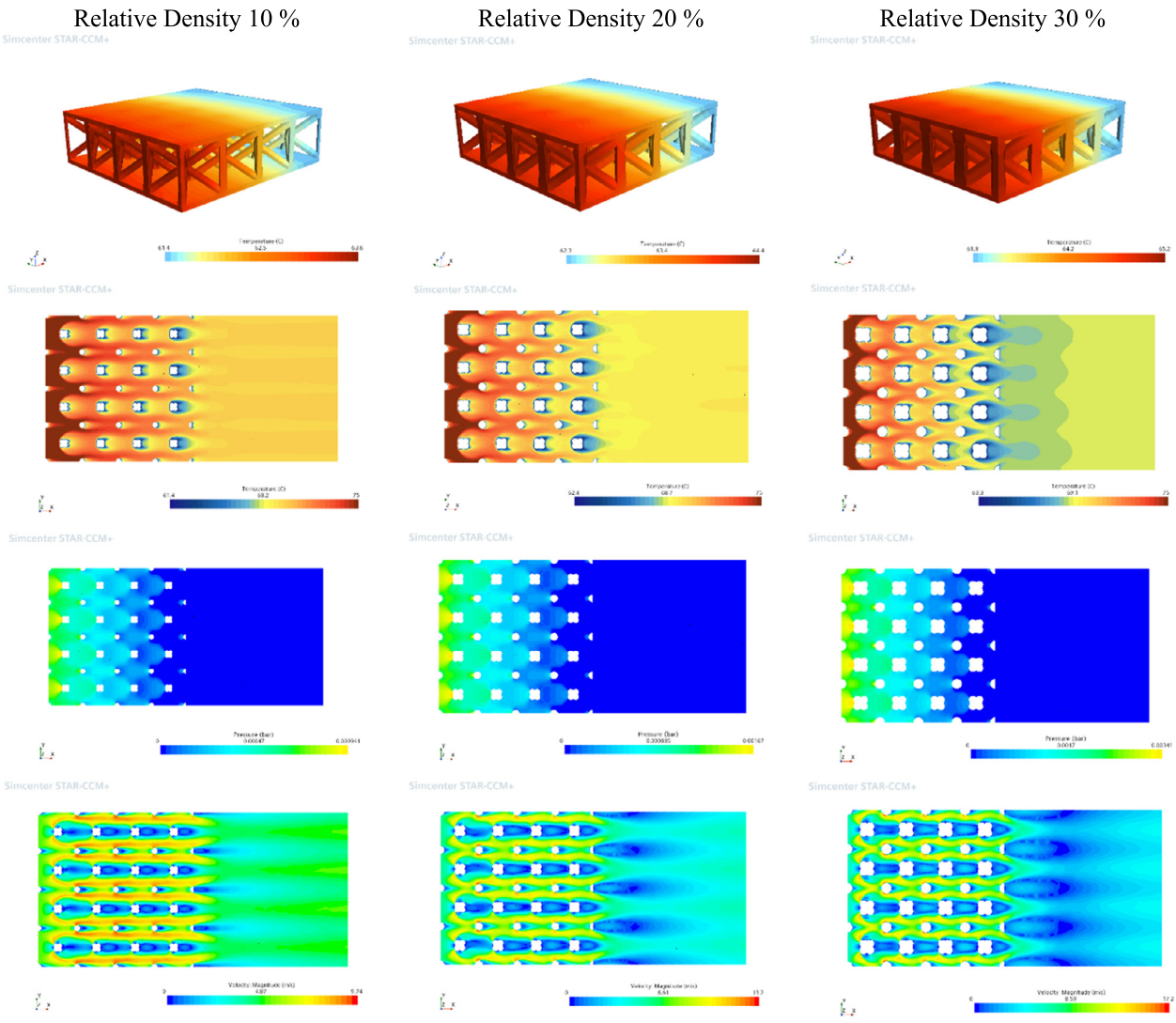

Fig. 15. Bccz 10 mm simulation: (a) plate temperature, (b) flow temperature, (c) static pressure, (d) flow velocity.

5.1.3. Cell size 12 mm

See Fig. 16.

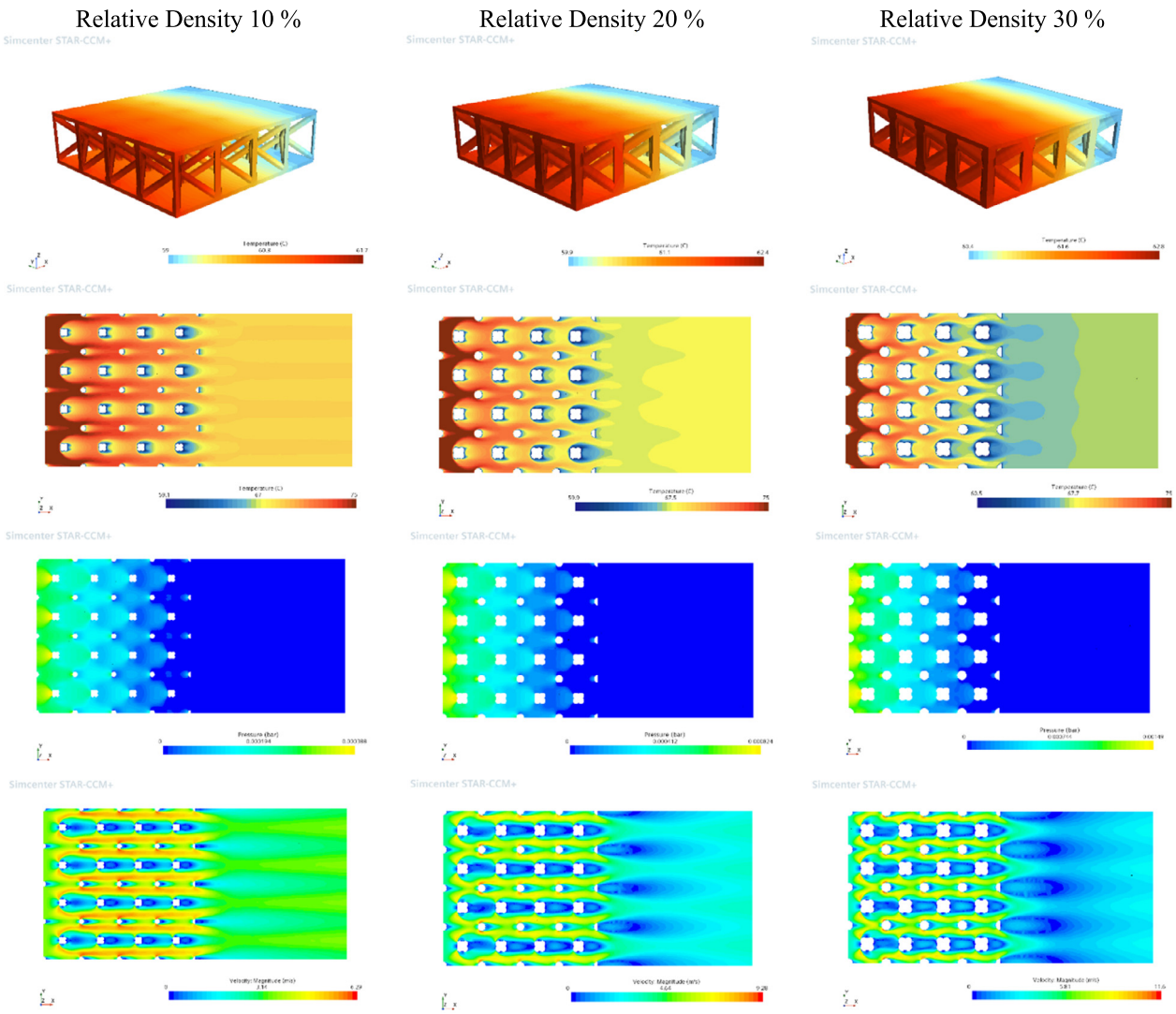

Fig. 16. Bccz 12 mm simulation: (a) plate temperature, (b) flow temperature, (c) static pressure, (d) flow velocity.

5.2. Rhombic

5.2.1. Cell size 8 mm

See Fig. 17.

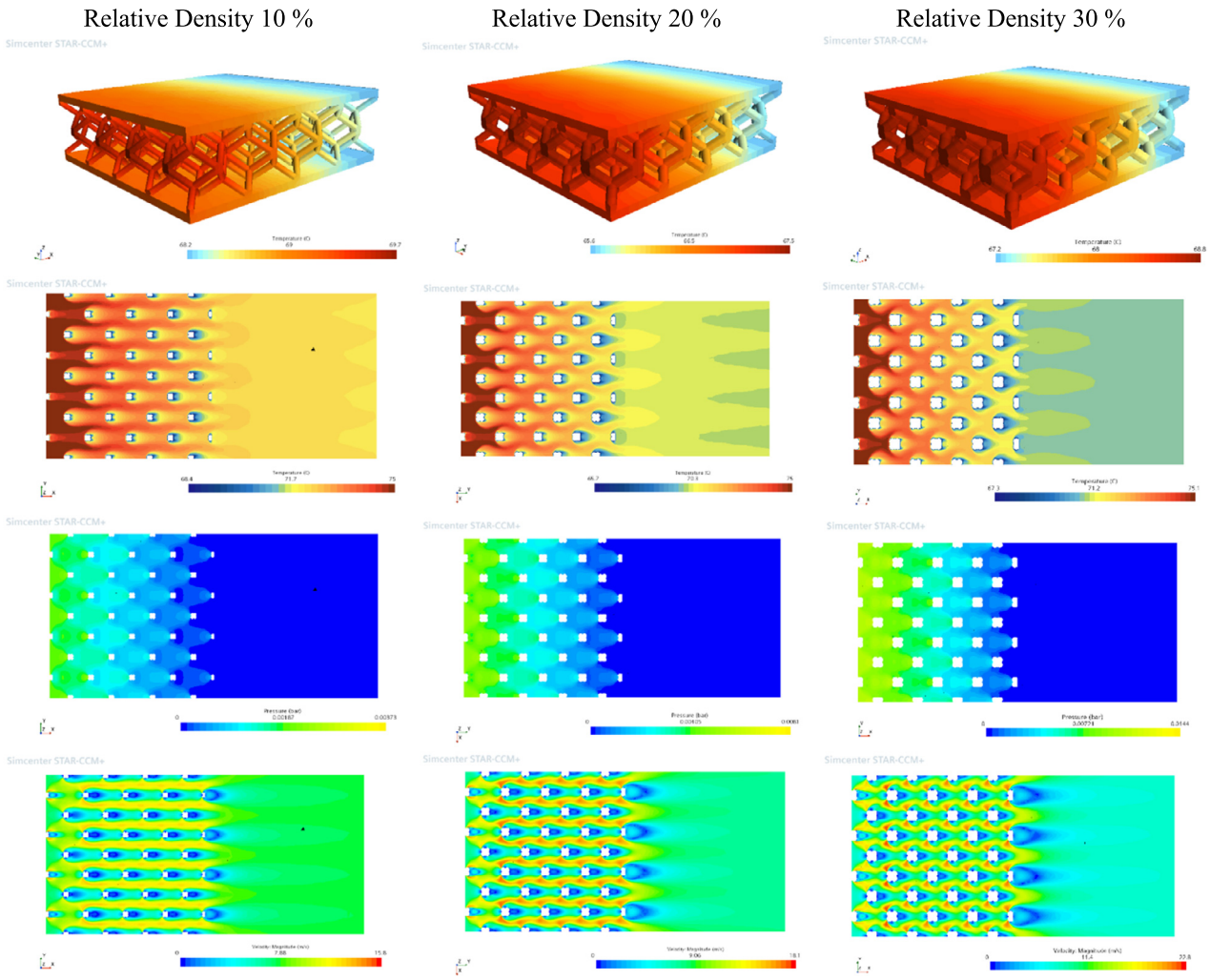

Fig. 17. Rhombic 8 mm simulation: (a) plate temperature, (b) flow temperature, (c) static pressure, (d) flow velocity.

5.2.2. Cell size 10 mm

See Fig. 18.

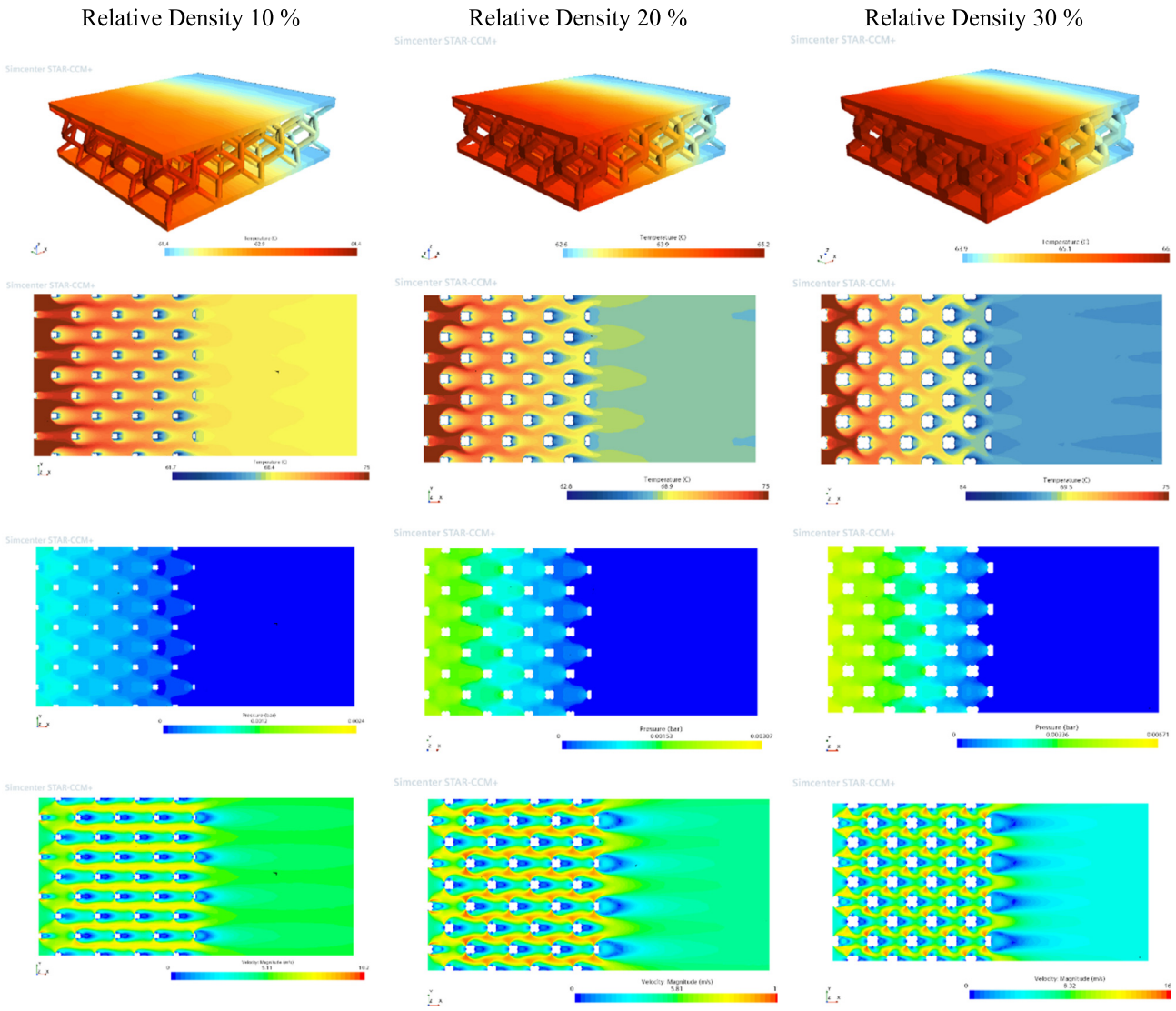

Fig. 18. Rhombic 10 mm simulation: (a) plate temperature, (b) flow temperature, (c) static pressure, (d) flow velocity.

5.2.3. Cell size 12 mm

See Fig. 19.

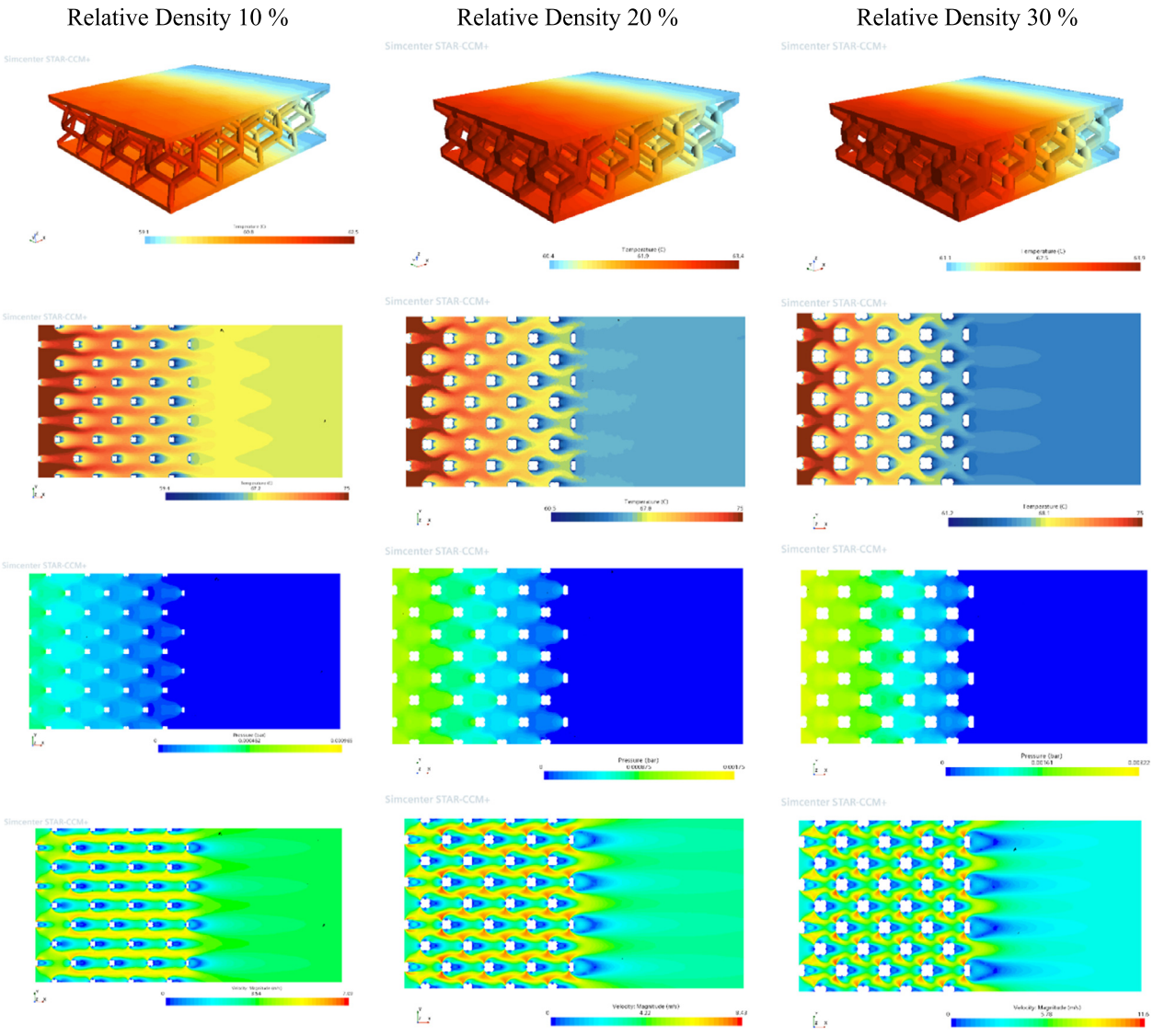

Fig. 19. Rhombic 12 mm simulation: (a) plate temperature, (b) flow temperature, (c) static pressure, (d) flow velocity.

5.3. Octet

5.3.1. Cell size 8 mm

See Fig. 20.

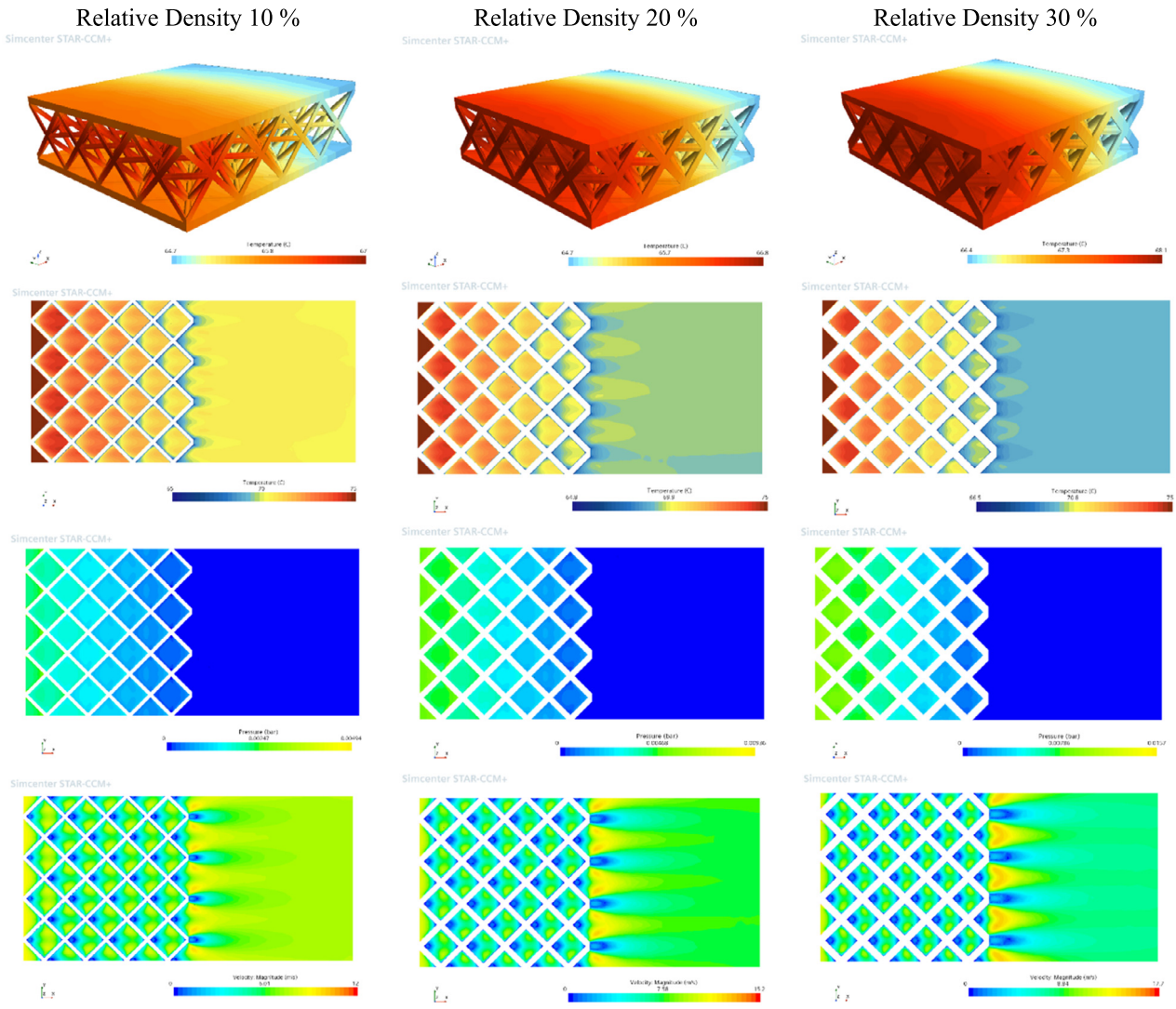

Fig. 20. Octet 8 mm simulation: (a) plate temperature, (b) flow temperature, (c) static pressure, (d) flow velocity.

5.3.2. Cell size 10 mm

See Fig. 21.

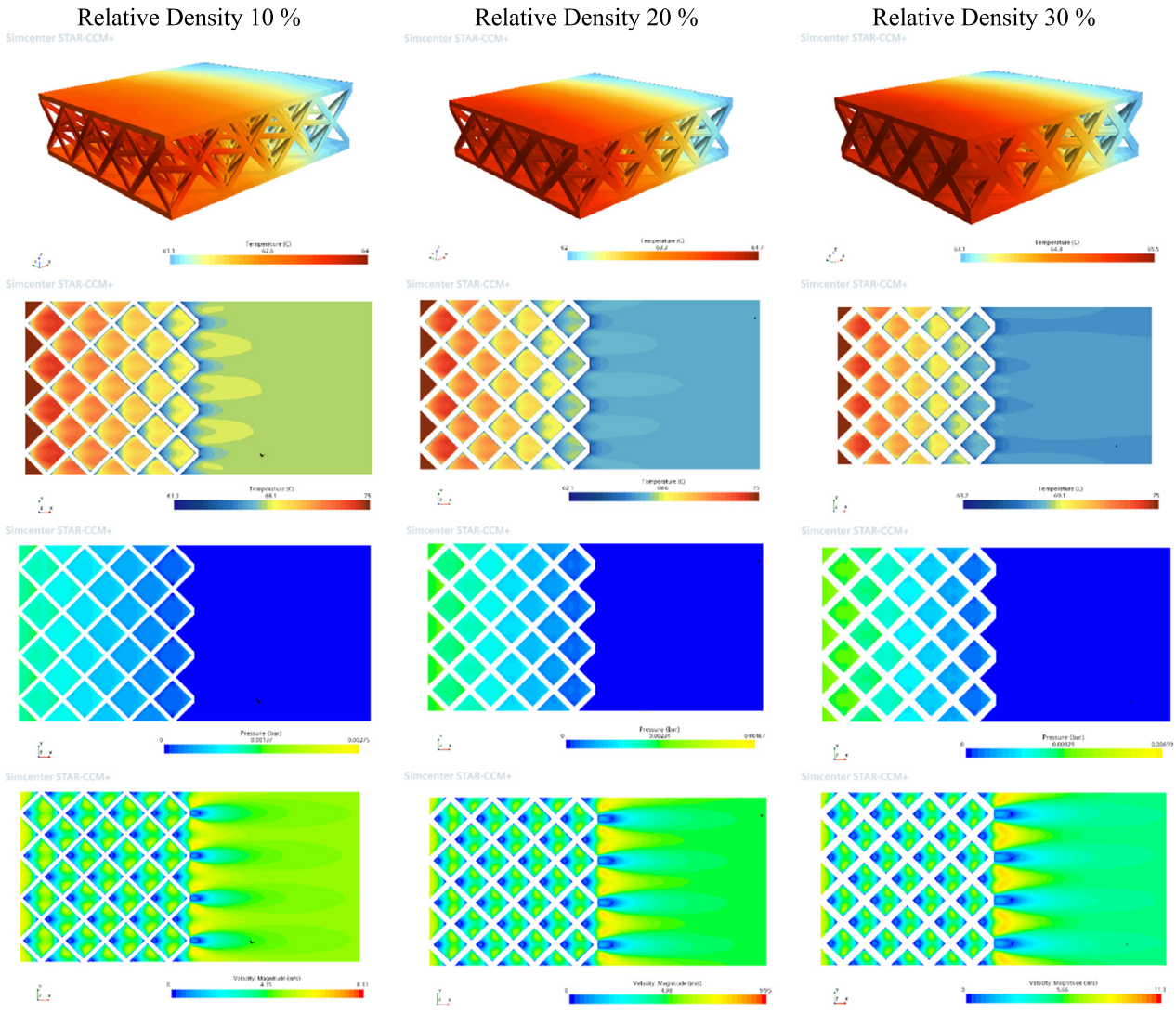

Fig. 21. Octet 10 mm simulation: (a) plate temperature, (b) flow temperature, (c) static pressure, (d) flow velocity.

5.3.3. Cell size 12 mm

See Fig. 22.

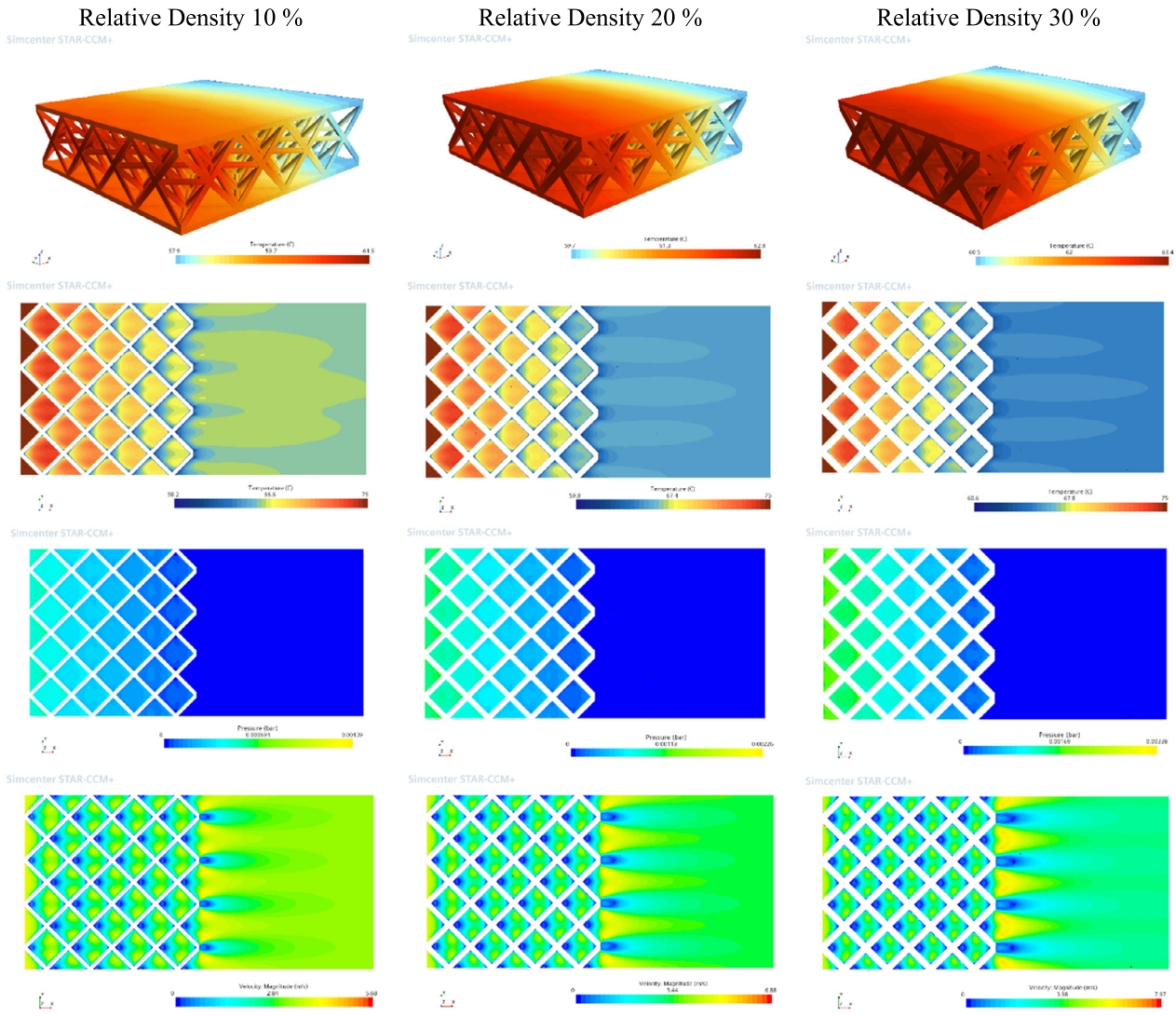

Fig. 22. Fig. 13 Octet 12 mm simulation: (a) plate temperature, (b) flow temperature, (c) static pressure, (d) flow velocity.

6. Appendix B Contour plot

6.1. Bccz

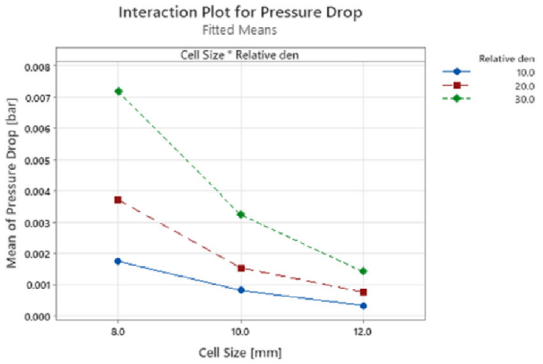

(a)

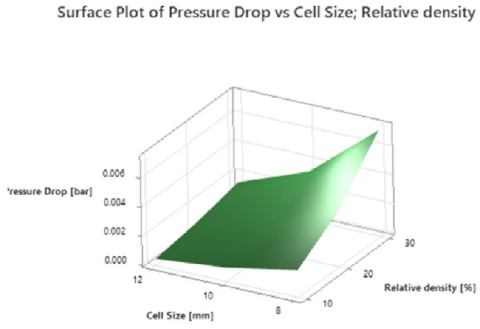

(b)

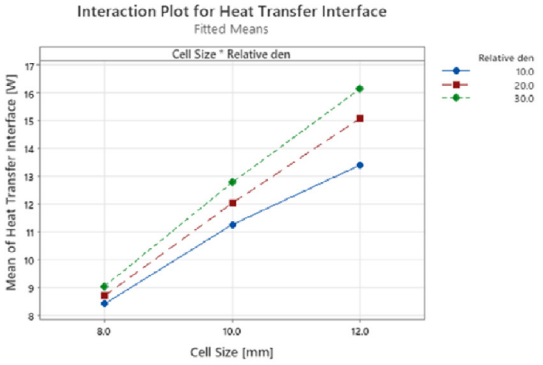

(c)

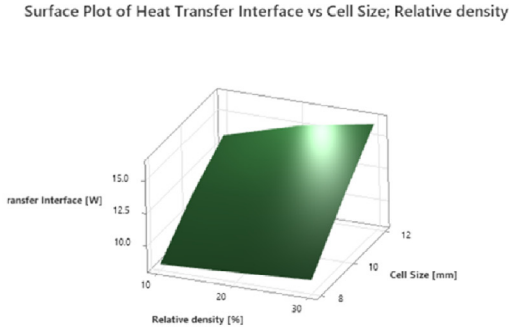

(d)

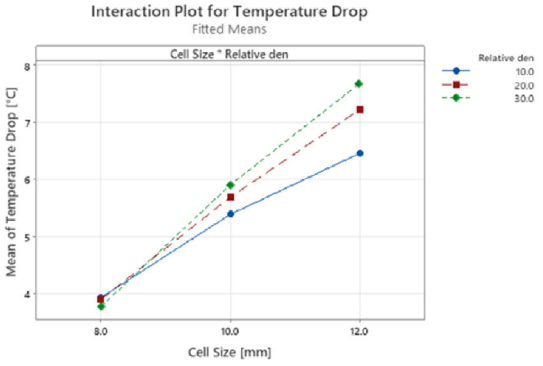

(e)

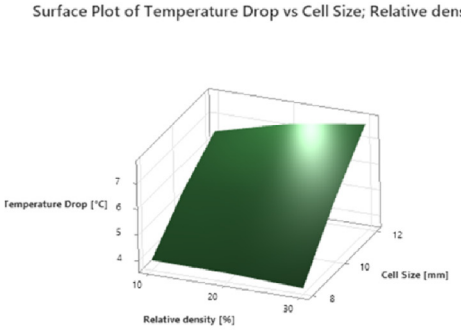

(f)

6.2. Rhombic

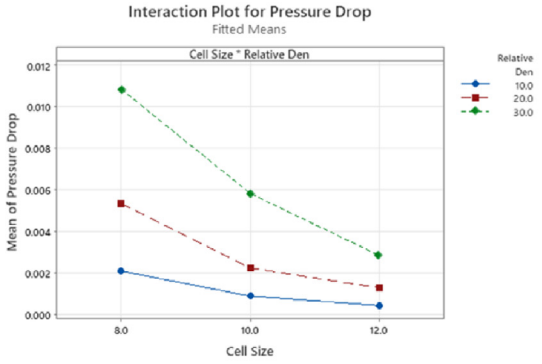

(a)

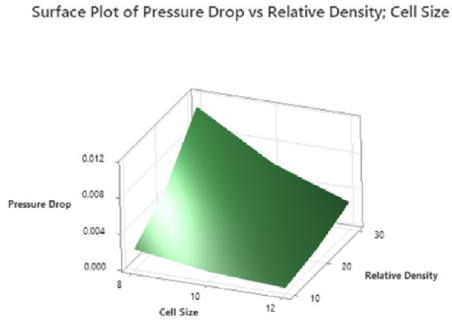

(b)

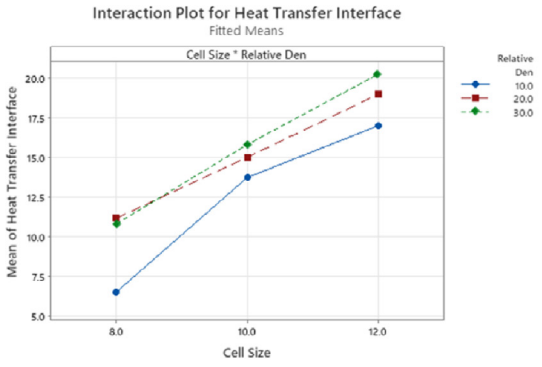

(c)

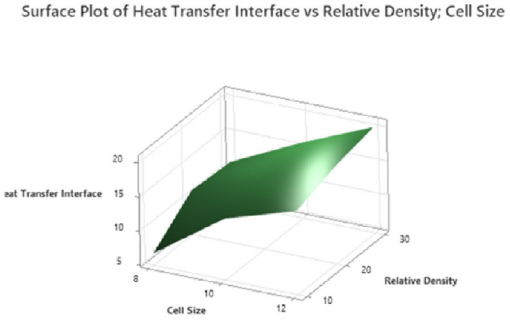

(d)

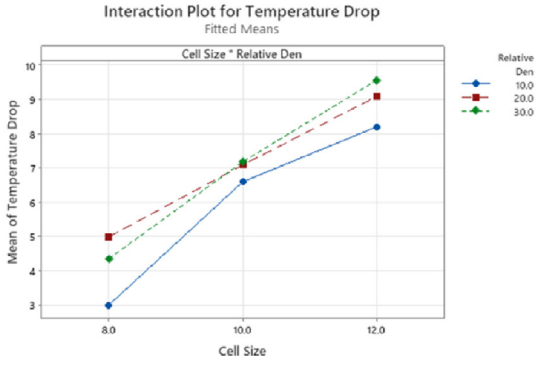

(e)

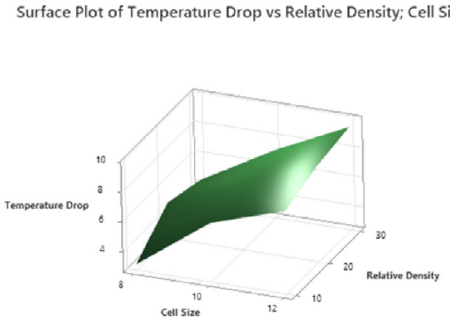

(f)

6.3. Octet

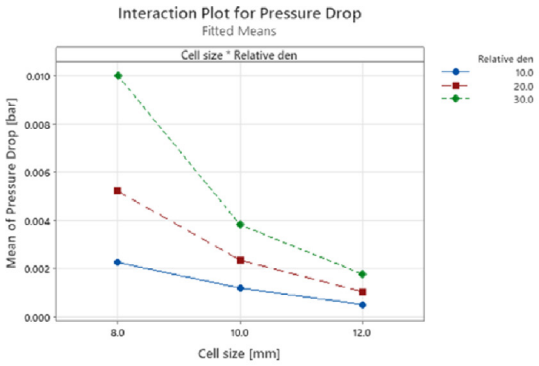

(a)

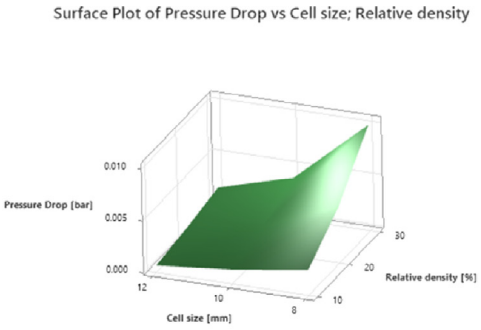

(b)

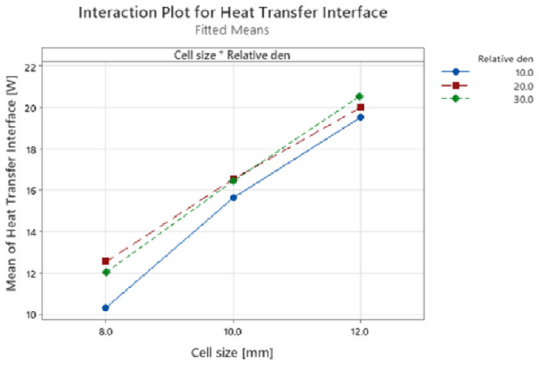

(c)

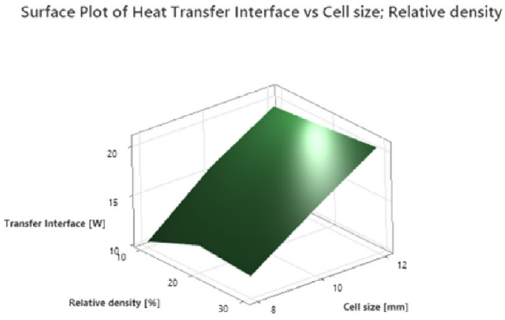

(d)

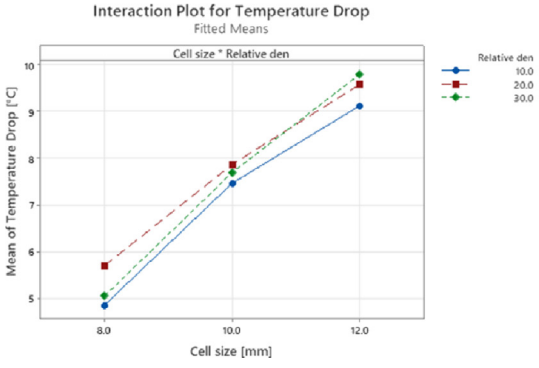

(e)

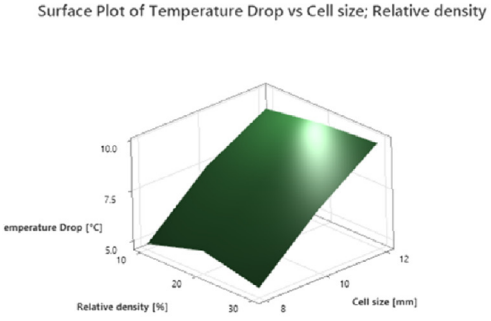

(f)

Declaration of competing interest

The authors declare that they have no known competing financial interests or personal relationships that could have appeared to influence the work reported in this paper.

Data availability

No data was used for the research described in the article.

References

[1] IPCC, IPCC Fifth Assessment Synthesis Report-Climate Change 2014 Synthesis Report, IPCC Fifth Assess. Synth. Report-Climate Chang. 2014 Synth. Rep, 2014.

[2] D.S. Lee, et al., Aviation and global climate change in the 21st century, Atmos. Environ. 43 (2009) 22–23, https://doi.org/10.1016/j.atmosenv.2009.04.024.

[3] P.M. Peeters, J. Middle, A. Hoolhorst, Fuel efficiency of commercial aircraft: an overview of historical and future trends, Natl. Aerosp. Lab. NLR Amsterdam (2005).

[4] M. Masiol, R.M. Harrison, Aircraft engine exhaust emissions and other airport-related contributions to ambient air pollution: a review, Atmos. Environ. 95 (2014) 409–455.

[5] S.K. Thomas, R.P. Cassoni, C.D. MacArthur, Aircraft anti-icing and de-icing techniques and modeling, J. Aircr. (1996), https://doi.org/10.2514/3.47027.

[6] Jonathan T. Salisbury, Microwave deicing and anti-icing system for aircraft, US5615849A, 1995.

[7] M. Mohseni, A. Amirfazli, A novel electro-thermal anti-icing system for fiber-reinforced polymer composite airfoils, Cold Reg. Sci. Technol. 87 (2013), https://doi.org/10.1016/j.coldregions.2012.12.003.

[8] P.M. Carlo Giovanni Ferro, Sara Varetti, Fabio Vitti, Thermal anti ice system integrated in the structure and method for its fabrication, 102016000098196,

2016 [Online]. Available: https://patents.google.com/patent/US20200031479A1/en.
[9] M.F. Ashby, The properties of foams and lattices, Philos. Trans. R. Soc. A Math. Phys. Eng. Sci. 364 (1838) (2006) 15–30, https://doi.org/10.1098/rsta.2005.1678.
[10] A. Seharing, A.H. Azman, S. Abdullah, A review on integration of lightweight gradient lattice structures in additive manufacturing parts, Adv. Mech. Eng. 12 (6) (2020), https://doi.org/10.1177/1687814020916951.
[11] J. Luo, L. Chen, A. He, W. Tao, Topology optimization of convective heat transfer by the lattice Boltzmann method, Int. J. Numer. Methods Fluids 95 (3) (2023) 421–452.
[12] T. Maconachie, et al., SLM lattice structures: properties, performance, applications and challenges, Mater. Des. 183 (2019), https://doi.org/10.1016/j.matdes.2019.108137.
[13] J.M.A. Longo, Modelling of hypersonic flow phenomena, Crit. Technol. Hypersonic Veh. Dev. Technol. Lect. Ser. (2004) 10–14.
[14] L. Hao, D. Raymont, C. Yan, A. Hussein, P. Young, Design and additive manufacturing of cellular lattice structures, Innov. Dev. Virtual Phys. Prototyp. (May 2016) (2011) 249–254, https://doi.org/10.1201/b11341-40.
[15] D.C. Montgomery, Design and Analysis of Experiments, John Wiley & sons, Inc, Arizona, 1976, p. 684.
[16] R.H. Myers, D.C. Montgomery, C.M. Anderson-Cook, Response Surface Methodology: Process and Product Optimization Using Designed Experiments, John Wiley & Sons, 2016.
[17] G. Taguchi, D. Clausing, Robust quality, Harv. Bus. Rev. 68 (1) (1990) 65–75.
[18] D. Berengut, Statistics for Experimenters: Design, Innovation, and Discovery, Taylor & Francis, 2006.
[19] SLM Solutions Group AG, SLM®500. the high power machine for metal additive manufacturing, https://www.slm-solutions.com/en/products-and-solutions/machines/slm-500/, 2023.
[20] M. Ashby, L. Gibson, Cellular Solids: Structure and Properties, Cambridge Univ. Press, 1999.
[21] J. Vojislav Petrovic, Juan Vicente Haro, Olga Jordá, Javier Delgado, L.P. Ramón Blasco, Additive layer manufacturing: state of the art in industrial applications through case studies, Int. J. Prod. Res. (2011).
[22] K. Boomsma, D. Poulikakos, On the effective thermal conductivity of a three-dimensionally structured fluid-saturated metal foam, Int. J. Heat Mass Transf. 44 (4) (2001) 827–836.
[23] A. Bhattacharya, V.V. Calmidi, R.L. Mahajan, Thermophysical properties of high porosity metal foams, Int. J. Heat Mass Transf. 45 (2002) 1017–1031.
[24] A.F. Bastawros, A.G. Evans, H.A. Stone, Evaluation of Cellular Metal Heat Transfer Media, Harvard University, Cambridge, 1999.
[25] M. Kaviany, Principles of Heat Transfer in Porous Media, second ed., Springer-Verlag, New York, 1995.
[26] C.G. Ferro, et al., Design and characterization of trabecular structures for an anti-icing sandwich panel produced by additive manufacturing, J. Sandw. Struct. Mater. 22 (4) (2020), https://doi.org/10.1177/1099636218780513.
[27] C.G. Ferro, S. Varetti, G. De Pasquale, P. Maggiore, Lattice structured impact absorber with embedded anti-icing system for aircraft wings fabricated with additive SLM process, Mater. Today Commun. 15 (2018), https://doi.org/10.1016/j.mtcomm.2018.03.007.
[28] Littlematt, Pneumatic anti ice, https://commons.wikimedia.org/wiki/File:Horizon_Air_Q400_deicing_boot.JPG.
[29] C. Zilio, L. Patricelli, Aircraft anti-ice system: evaluation of system performance with a new time dependent mathematical model, Appl. Therm. Eng. 63 (1) (2014), https://doi.org/10.1016/j.applthermaleng.2013.10.048.
[30] M. Papadakis, S.H. Wong, H.W. Yeong, S.C. Wong, G.T. Vu, Icing tunnel experiments with a hot air anti-icing system, https://doi.org/10.2514/6.2008-444, 2008.
[31] C. Ferro, et al., A robust multifunctional sandwich panel design with trabecular structures by the use of additive manufacturing technology for a new de-icing system, Technologies 5 (2) (2017) 35, https://doi.org/10.3390/technologies5020035.
[32] S. Zhao, S.J. Li, W.T. Hou, Y.L. Hao, R. Yang, R.D.K. Misra, The influence of cell morphology on the compressive fatigue behavior of Ti-6Al-4V meshes fabricated by electron beam melting, J. Mech. Behav. Biomed. Mater. 59 (2016) 251–264, https://doi.org/10.1016/j.jmbbm.2016.01.034.
[33] T. Tancogne-Dejean, A.B. Spierings, D. Mohr, Additively-manufactured metallic micro-lattice materials for high specific energy absorption under static and dynamic loading, Acta Mater. 116 (2016) 14–28, https://doi.org/10.1016/j.actamat.2016.05.054.
[34] EOS GmbH - Electro Optical Systems, Material data sheet: EOS aluminium AlSi10Mg, 49 (2014) 1–5.
[35] Siemens and CD-Adapco, User Guide, STAR CCM+, version 12.06.011, 2012.
[36] Carlo Giovanni Ferro, Multidisciplinary analysis of a novel anti-icing system for a fixed wing UAV, 2019.
[37] V.A. Kurganov, Heat transfer, Thermopedia (2001).